Bioorganic Chemistry 150 (2024) 107589

Contents lists available at ScienceDirect

Bioorganic Chemistry

journal homepage: www.elsevier.com/locate/bioorg

Triazole derivatives inhibit the VOR complex-mediated nuclear transport of extracellular particles: Potential application in cancer and HIV-1 infection

Daniela Carbone [a,1], Mark F. Santos [b,1], Denis Corbeil [c,d], Giulio Vistoli [e], Barbara Parrino [a,*], Jana Karbanová [c,d], Stella Cascioferro [a], Camilla Pecoraro [a], Jodi Bauson [b], Waleed Eliwat [b], Feryal Aalam [b], Girolamo Cirrincione [a], Aurelio Lorico [b,*,2], Patrizia Diana [a,2]

[a] Department of Biological, Chemical, and Pharmaceutical Sciences and Technologies (STEBICEF), University of Palermo, Palermo, Italy
[b] Touro University Nevada College of Osteopathic Medicine, Henderson, NV, USA
[c] Biotechnology Center (BIOTEC) and Center for Molecular and Cellular Bioengineering, Technische Universität Dresden, Dresden, Germany
[d] Tissue Engineering Laboratories, Medizinische Fakultät der Technischen Universität Dresden, Dresden, Germany
[e] Department of Pharmaceutical Sciences, University of Milan, Milan, Italy

ARTICLE INFO

Keywords:
Anti-cancer
Anti-HIV-1
Exosome
Itraconazole derivative
Microvesicle
VOR complex

ABSTRACT

Extracellular vesicles (EVs) appear to play an important role in intercellular communication in various physiological processes and pathological conditions such as cancer. Like enveloped viruses, EVs can transport their contents into the nucleus of recipient cells, and a new intracellular pathway has been described to explain the nuclear shuttling of EV cargoes. It involves a tripartite protein complex consisting of vesicle-associated membrane protein-associated protein A (VAP-A), oxysterol-binding protein (OSBP)-related protein-3 (ORP3) and late endosome-associated Rab7 allowing late endosome entry into the nucleoplasmic reticulum. Rab7 binding to ORP3-VAP-A complex can be blocked by the FDA-approved antifungal drug itraconazole. Here, we design a new series of smaller triazole derivatives, which lack the dioxolane moiety responsible for the antifungal function, acting on the hydrophobic sterol-binding pocket of ORP3 and evaluate their structure–activity relationship through inhibition of VOR interactions and nuclear transfer of EV and HIV-1 cargoes. Our investigation reveals that the most effective compounds that prevent nuclear transfer of EV cargo and productive infection by VSV-G-pseudotyped HIV-1 are those with a side chain between 1 and 4 carbons, linear or branched (methyl) on the triazolone region. These potent chemical drugs could find clinical applications either for nuclear transfer of cancer-derived EVs that impact metastasis or viral infection.

1. Introduction

Extracellular vesicles (EVs) are highly heterogeneous, membrane-encapsulated particles released by cells into the extracellular environment [1–4]. Several types of EVs have been identified and among them there are two major classes, exosomes and ectosomes [5]. The former are of endosomal-origin and they are released after the fusion of multivesicular bodies with the cell membrane, while the latter

Abbreviations: BSA, bovine serum albumin; CLSM, confocal laser-scanning microscopy; DMSO, dimethyl sulfoxide; EV, extracellular vesicles; HIV-1, human immunodeficiency virus type 1; GFP, green fluorescent protein; kDa, kilodalton; ICZ, itraconazole; MOI, multiplicity of infection; MTS, 3-(4,5-dimethylthiazol-2-yl)-5-(3-carboxymethoxyphenyl)-2-(4-sulfophenyl)–2H-tetrazolium; NEI, nuclear envelope invagination; NR, nucleoplasmic reticulum; ORD, OSBP-related domain; ORP3, oxysterol-binding protein-related protein 3; OSBP, oxysterol-binding protein; PFA, paraformaldehyde; PIC, pre-integration complex; RFP, red fluorescent protein; RT, room temperature; S.D, standard deviation; SUN, Sad1 and UNC84; SUN2, SUN domain-containing protein 2; VAP-A, vesicle-associated membrane protein-associated protein A; VSV-G, vesicular stomatitis virus G.

* Corresponding authors.
E-mail addresses: daniela.carbone@unipa.it (D. Carbone), msantos17@touro.edu (M.F. Santos), denis.corbeil@tu-dresden.de (D. Corbeil), giulio.vistoli@unimi.it (G. Vistoli), barbara.parrino@unipa.it (B. Parrino), jana.karbanova@tu-dresden.de (J. Karbanová), stellamaria.cascioferro@unipa.it (S. Cascioferro), camilla.pecoraro@unipa.it (C. Pecoraro), Jbauson@student.touro.edu (J. Bauson), weliwat@student.touro.edu (W. Eliwat), farizeh.aalam@gmail.com (F. Aalam), girolamo.cirrincione@unipa.it (G. Cirrincione), alorico@touro.edu (A. Lorico), patrizia.diana@unipa.it (P. Diana).

[1] These authors contributed equally.
[2] These authors are senior authors for their respective disciplines.

https://doi.org/10.1016/j.bioorg.2024.107589
Received 24 April 2024; Received in revised form 20 June 2024; Accepted 22 June 2024
Available online 23 June 2024
0045-2068/© 2024 The Authors. Published by Elsevier Inc. This is an open access article under the CC BY-NC-ND license (http://creativecommons.org/licenses/by-nc-nd/4.0/).

are of plasma membrane-origin and bud or shed into the extracellular milieu. Both have been shown to contain a wide variety of bioactive cargoes (proteins, nucleic acids, lipids) that can be transferred to other cells playing an essential role in intercellular communication under physiological states [6–10]. They are also involved in different pathological conditions that lead to production of disease-specific EVs, such as in cancer [11,12]. In the tumor microenvironment, due to their specific cargoes, EVs promote cancer cells progression, angiogenesis and metastasis [13]. Interestingly, the homology between exosomal pathways and the retroviral cycle, as postulated by the Trojan exosome hypothesis [14], allows retroviruses, such as human immunodeficiency virus type 1 (HIV-1), to utilize the exosomal pathway for successful cell infection. In particular, the biogenesis of exosomes and their potential fusion and/or uptake via endocytosis by recipient cells have many commonalities with the retroviral life cycle [15]. As a consequence, retroviruses also insert viral parts or whole virions inside EVs and that helps spreading viral infection [16].

A new protein complex, called VOR (acronym for its three protein components), namely vesicle-associated membrane protein-associated protein A (VAP-A) located in the outer nuclear membrane, cytoplasmic oxysterol-binding protein (OSBP)-related protein-3 (ORP3, also known as OSBP-Like 3) and late endosome-associated Rab7, has been shown to be pivotal in the nuclear transfer of cargo proteins transported by EVs or enveloped HIV-1 [17–19]. In these processes, a minute fraction of Rab7^{+} late endosomes containing endocytosed particles are transported to the perinuclear region where they are incorporated into the nucleoplasmic reticulum (NR) [20,21]. In this confined subcellular area, the fusion of endocytosed particles with the endosomal membrane allows the release of their cargoes in the vicinity of the nuclear pores, thus facilitating their nuclear transfer [17,19,20]. These molecular and cellular processes depend on both VAP-A and ORP3, as their silencing prevented the localization of late endosomes in NR, and subsequent nuclear transfer of endocytosed particle-derived components [17–19]. Incubation of cells with the FDA-approved antifungal drug itraconazole (ICZ), which acts on ORP3, also blocked these events [18,19].

Like other members of OSBP protein family, ORP3 is composed of distinct domains, including a pleckstrin homology (PH) domain in the *N*-terminal region, two FFAT (two phenylalanines (FF) in an acidic tract) motifs in the middle part, and a sterol-binding OSBP-related domain (ORD) in the C-terminal region that regulate its various protein and lipid interactions, subcellular localization and function [22]. OSBP proteins are involved in various activities ranging from lipid sensing and trafficking to sterol homeostasis and cell signaling. At membrane contact sites that bridge distinct organelles [23,24], OSBP proteins play a critical role in the non-vesicular exchange of lipids between adjacent membranes [25,26].

At the plasma membrane endoplasmic reticulum (ER) contact sites, the binding of ORP3 to ER-associated VAP-A and the small GTPase R-Ras regulated cell adhesion and migration by stimulating the R-Ras signaling and β1-integrin activity [27,28]. A similar tripartite interaction occurs at the contact zone between the outer nuclear membrane (ONM) and late endosomes involving the small GTPase Rab7 [19]. While the interaction of ORP3 with VAP-A is mediated by its FFAT motifs in a phosphorylation dependent mechanism [18,27–29], its binding to Rab7 remains to be identified. In contrast to ORP1L, another member of OSBP protein, ORP3 does not contain an ankyrin repeat region, which could mediate Rab7 interaction [30]. The involvement of the R-Ras binding site in ORP3 remains to be evaluated [27,28]. Nevertheless, close contact of ORP3 with Rab7 can occur when its PH domain binds to certain phosphoinositides associated with target late endosomes [25]. Like several other OSBP proteins, ORP3 was shown to bind directly to cholesterol and 25-hydroxycholesterol (25-hc) [31]. The sterol-sensing ORD may also influence its interaction with Rab7 [25]. Indeed, ICZ specifically acts via its triazolone region (Fig. 1) on the hydrophobic sterol-binding pocket of ORP3 ORD, resulting in the lack of Rab7 binding to ORP3-VAP-A complexes. Its inhibitory effect can be suppressed in a dose-dependent manner by the addition of 25-hc [18]. Unlike ICZ, neither hydroxy-ICZ, its major metabolite, which maintains the anti-fungal activity, nor ketoconazole have the property to disrupt the VOR complex (Fig. 1) [18].

The possibility that cell communication at the nuclear level between cancer and stromal/immune cells in the tumor microenvironment and the nuclear entry of HIV-1 in recipient cells could be inhibited by small molecules prompted us to develop inhibitors of potential clinical utility. We initially designed the 1,2,4-triazolone derivative **2a**, a small chemical compound mimicking the triazolone region of ICZ, but lacking the dioxolane portion responsible for the anti-fungal activity [18]. In addition to the absence of moieties that inhibit other cellular targets not related to the VOR complex, this smaller drug has only one chiral center (compared to three in ICZ), thus avoiding many of the off-target effects of ICZ. The molar concentration required to interfere with VOR complex formation is similar to that of ICZ, however, due to its ~ 3-fold lower molecular weight, the absolute amount of **2a** required to achieve the same effect was considerably less. Interestingly, homology modeling analyses of the active group of ICZ and **2a** with the ORD domain of other ORP proteins (i.e., OSBP, ORP1, ORP2, ORP4, ORP6, ORP7, and ORP9) showed that a key triad of residues (Arg558, Tyr593 and Trp653) of ORP3 is present and/or in a configuration accessible for drug binding only in ORP7, indicating **2a** specificity and limited toxicity [18].

In the present study, we designed a new series of small derivatives acting on the hydrophobic sterol-binding pocket of ORP3 and evaluated their structure–activity relationship (SAR) through inhibition of VOR interactions. As a proof of concept of their actions, we evaluated the nuclear transfer of cargo proteins carried by extracellular particles such as EVs or enveloped HIV-1 virus.

2. Results and discussion

2.1. Chemistry

The VOR complex disruption by ICZ and compound **2a** prompted us to study other related molecules that met the minimum requirements to interfere with the VOR complex. For this purpose, the ICZ molecule was dissected into three parts: i) the portion of the dioxolane ring bearing a di-chlorophenyl ring and a triazole nucleus; ii) the linker moiety, constituted by two benzene rings separated by a piperazine system

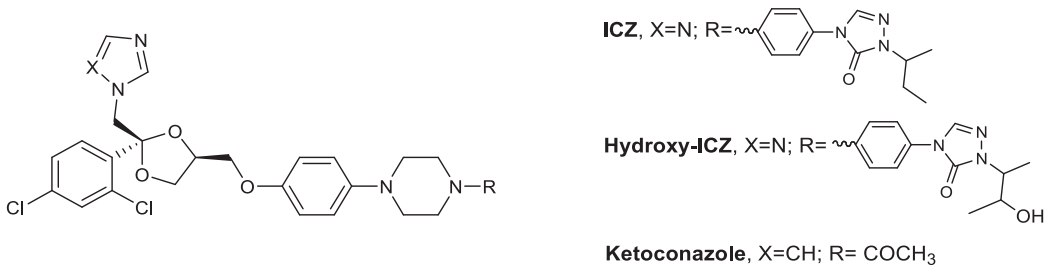

Fig. 1. Chemical structures of itraconazole, hydroxy-itraconazole and ketoconazole.

which forms two N—C bonds with both rings; and iii) a triazolone ring bearing a *sec*-butyl side chain at the other end of the molecule (Fig. 2). The overall aim is the modification of each portion leaving the other two unchanged. Here, we focused on modifications in the last part, the triazolone ring.

The 1,2,4-triazol-3-one derivatives **2b** to **2y** were then synthesized using chemical procedures similar to those reported for the formulation of compound **2a** [18]. In particular, the reaction of anilines with triethyl orthoformate, *p*-toluenesulfonic acid, methyl carbazate and a solution of sodium methoxide in methanol led to a series of intermediate products **1** (Scheme 1, step i), which were subsequently subjected to *N*-alkylation reaction, performed in dimethyl sulfoxide (DMSO) using 18-crown-6 as catalyst (Scheme 1, step ii). In case of derivative **2h**, 4-nitroaniline was used as starting material to obtain, via **1e** intermediate, the related 1,2,4-triazol-3-one **2y** that was subjected to reduction using tin chloride in concentrated chloridric acid (Scheme 1, step iii). Compound **2a** was later to serve as a building block to bind to the piperazine nucleus of the linker to which analogues of the dioxolane portion were to be bound. Thus, this simple and inexpensive synthetic procedure and the possibility of introducing different substituents on the phenyl ring and a wide range of side chains in the triazolone portion led to the synthesis of a series of new compounds, in good to excellent yields.

In the twenty-five triazolone *N*-substituted derivatives (**2a-y**) herein reported, C1-C6 linear, branched or cyclic aliphatic side chains as well as hydroxyalkyl or alkyl-heterocyclic substituents were introduced. Moreover, the phenyl ring at the triazolone N4 nitrogen was substituted with halogens (F, Cl, Br) at different positions and with an amino group at position 4.

2.2. Biological evaluation

2.2.1. Inhibition of the VOR complex interactions

In a recent study, both compounds **1a** and **2a** were evaluated for their ability to inhibit the interactions of VOR proteins, notably the binding of Rab7 to ORP3-VAP-A complexes [18]. Like ICZ, compound **2a** inhibited the VOR complex *in vivo*, i.e. when applied to cultured cells, or *in vitro*, i.e. when applied to detergent cell lysates, whereas compound **1a** was completely devoid of such inhibitory activity. Computer modelling studies evidenced interactions of compound **2a** comparable to those shown by ICZ in the deepest cavity of a homology model of ORP3 ORD protein (see also below) [18]. Importantly, compound **2a** showed a much better toxicity profile than ICZ, particularly on primary cells (see below section 2.2.4).

To assess experimentally the impact of novel chemical compounds on the VOR complex integrity, we used a co-immunoisolation protocol based on paramagnetic-bead separation [19]. Human ORP3 was used as bait by applying a monoclonal antibody (Ab) against it. As reference host cells, we used non-metastatic SW480 human colon adenocarcinoma cells in which inhibition of VOR complex formation prevented their malignant transformation mediated by EVs derived from their metastatic counterparts, i.e. SW620 cells [18]. For this purpose, SW480 cells were incubated with ICZ or drug derivatives at different concentrations (2.5, 5.0, 7.5 and 10 μM) for a period of 5 h at 37 °C. As a negative control, cells were incubated with the solvent vehicle (DMSO) only. Afterward, detergent cell lysates were prepared and ORP3 protein was immunoisolated. The recovered materials were then probed by immunoblotting for ORP3, VAP-A, and Rab7 (Fig. 3A). Alternatively, the drugs were added directly on detergent cell lysates for 30 min on ice prior to the co-immunoisolation. For all compounds, a concentration of 2.5 μM had no impact on the ORP3-Rab7 interaction. However, the latter was progressively and strongly impaired when higher concentrations of ICZ or certain compounds (e.g., **2a**, **2j**) were applied to the living cells or detergent cell lysates. In contrast, a mild effect of **2e** on the ORP3-Rab7 interaction was observed, whereas no effect was seen with **1b** and **2s** (Fig. 3A). None of the drugs blocked the ORP3-VAP-A interaction. The IC_{50} values for the inhibition of the interaction between OPR3 and Rab7 were then calculated using a simple linear regression, as shown for **2j** (Fig. 3B), for all compounds and both treatment protocols (Fig. 3C). Irrespective of the protocols applied (living cells versus cell lysates detergents), the analysis revealed that the potency of the compounds, as evaluated by their IC_{50}, can be classified into four categories, from those similar to ICZ (IC_{50} of about 5.0), intermediates (IC_{50} of about 6–8 and 9–15), and to those with no effect (Fig. 3C). The fact that the trend for all compounds is parallel when added to cells compared to detergent cell lysates suggests that drug passage across the plasma membrane is not a rate-limiting factor. Furthermore, these data could also rule out the drugs having an impact on late endosome transport to the nuclear region, an action reported for ICZ [32,33], thereby excluding that the inhibition of the VOR complex is not due to the absence of Rab7 in the vicinity of the ORP3-VAP-A complex [18].

As previously shown, compound **2a** showed a similar IC_{50} as ICZ [18]. By increasing the side chain by one carbon unit (**2n**), a decrease of the inhibition was observed. A more marked decrease in activity was observed in compound **2o** bearing a side chain with one carbon unit less.

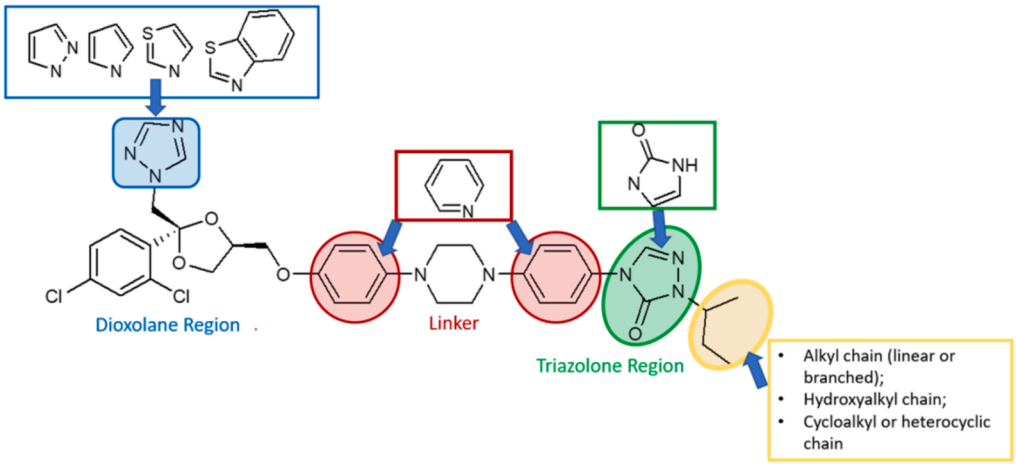

Fig. 2. Optimization of lead compound itraconazole. Various regions of itraconazole are targeted for optimization: Substitution of the triazole moiety of the dioxolane portion with other 5-membered heterocycles also benzo-annelated (blue); Substitution of the two phenyl rings with one or two pyridine moieties (red); Substitution of the triazole ring of the triazolone region with an imidazole ring and substitution of the side chain (yellow) as indicated. In this study, we focused on the latter region, where numerous triazole derivative analogues were prepared (see below Scheme 1). (For interpretation of the references to colour in this figure legend, the reader is referred to the web version of this article.)

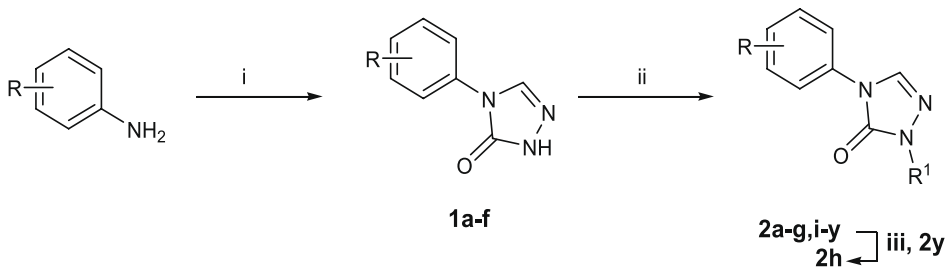

Compound	R	R[1]	Yield %	Compound	R	R[1]	Yield %
1a	4-Cl	-	99	**2k**	4-Cl	$CH_2CH_2CH_3$	98
1b	2-Cl	-	85	**2l**	2-Cl	$CH_2CH_2CH_3$	83
1c	4-F	-	99	**2m**	3-Cl	$CH_2CH_2CH_3$	90
1d	4-Br	-	98	**2n**	4-Cl	$CH(CH_3)CH_2CH_2CH_3$	98
1e	4-NO_2	-	98	**2o**	4-Cl	$CH(CH_3)_2$	99
1f	3-Cl	-	89	**2p**	4-Cl	CH_2CH_2OH	87
2a	4-Cl	$CH(CH_3)CH_2CH_3$	99	**2q**	4-Cl	$CH_2CH_2CH_2OH$	89
2b	4-Cl	CH_3	99	**2r**	4-Cl	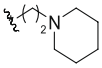	88
2c	4-Br	CH_2CH_3	98	**2s**	4-Cl	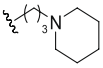	90
2d	4-F	CH_2CH_3	97	**2t**	4-Cl	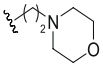	94
2e	4-Cl	CH_2CH_3	92	**2u**	4-Cl	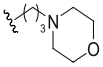	93
2f	3-Cl	CH_2CH_3	88	**2v**	4-Cl		97
2g	2-Cl	CH_2CH_3	86	**2w**	4-Cl		91
2h	4-NH_2	CH_2CH_3	90	**2x**	4-Cl		91
2i	4-F	$CH_2CH_2CH_3$	99	**2y**	4-NO_2	CH_2CH_3	98
2j	4-Br	$CH_2CH_2CH_3$	96				

Scheme 1. General synthetic pathway for the preparation of compounds **1a-f** and **2a-y**. **Reagents and conditions:** i) triethyl orthoformate, *p*-toluenesulfonic acid, methyl carbazate in methanol, 3 h, reflux; then sodium in methanol, 2–24 h, reflux; ii) Na_2CO_3, 18-crown-6, haloalkane, in dimethyl sulfoxide, 8 h, 60 °C; iii) conc. HCl, $SnCl_2$, 2 h at room temperature then aqueous NaOH (30 %).

Interestingly, compound **2k**, bearing a linear C3 alkyl chain, maintained a similar activity as **2a**. In contrast, compounds **2e**, bearing an ethyl side chain, and **2b**, bearing a methyl group, showed gradually diminished activities (IC_{50} on cell lysates = 9.66 and 73.98 μM, respectively), while **1a**, having no side chain, was completely inactive. The introduction of polar groups at the end of the side chain was detrimental for the inhibition activity. For example, hydroxypropyl derivative **2q** showed a significant decrease of activity (IC_{50} = 10.46 μM) compared with **2k** (IC_{50} = 4.67 μM). The hydroxyethyl derivative **2p** versus **2e** exhibited similar activity (IC_{50} = 9.81 and 9.66 μM, respectively).

The cycloalkyl side chains produced dramatic changes in the inhibition effect. While **2v** and **2w**, bearing 4- and 5-membered cycloalkyl

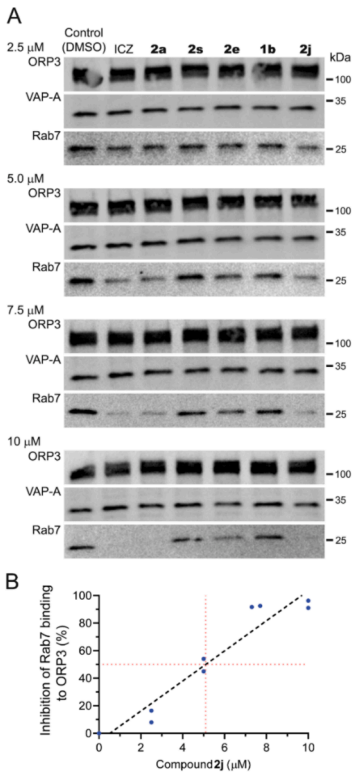

C

Compounds	IC_{50} on cells	IC_{50} on lysates
ICZ	5.11[a]	5.08
1a	no effect[b]	no effect
1b	no effect	no effect
1c	16.36	16.93
1d	11.45	21.33
2a	4.93	4.87
2b	no effect	73.98
2c	5.69	4.49
2d	5.21	5.14
2e	10.55	9.66
2f	6.65	5.43
2g	5.14	4.86
2h	7.01	5.91
2i	5.05	4.55
2j	5.23	5.10
2k	5.39	4.67
2l	5.28	4.55
2m	5.01	4.71
2n	6.19	6.51
2o	7.39	8.82
2p	11.92	9.81
2q	14.41	10.46
2r	12.77	13.54
2s	no effect	no effect
2t	no effect	no effect
2u	no effect	no effect
2v	8.89	8.47
2w	10.48	11.94
2x	no effect	74.43

[a]: μM
[b]: No effect is defined as having IC_{50} greater than 100 μM

Fig. 3. ICZ and its smaller triazole derivative analogues disrupt the interaction of VOR complex. **A-C** SW480 cells (A-C) or detergent cell lysates derived therefrom (C) were incubated with increasing concentration of ICZ or its analogues as indicated for 5 h at 37 °C (A-C) or 30 min at 4 °C (C), solubilized and subjected to co-immunoisolation using anti-ORP3 Ab followed by Protein G-coupled magnetic beads. DMSO was used as solvent vehicle control. The entire bound fractions were probed by immunoblotting for ORP3, VAP-A, and Rab7. Molecular weights (kDa) are indicated (A). Drug potency was determined for the inhibition of ORP3-Rab7 interaction (B, C). The ratio of Rab7/ORP3 immunoreactivities in treated samples relative to the control was determined as percent inhibition. Simple linear regression was then used to calculate IC_{50} from these immunoblotting data (B). Representative immunoblots (A) and a regression plot (B) are shown, while the IC_{50} of all drugs for both experimental protocols is displayed (C).

moieties, respectively, showed IC_{50} values of 8.47 and 11.94 μM, respectively, 6-membered **2x** was totally inactive. Also, the ethyl- and propyl-piperidine substituted compounds, **2r** and **2s**, had very poor inhibition activity or practically inactive, respectively (IC_{50} = 13.54 μM and *no effect*, respectively), as well as the corresponding morpholine derivatives **2t** and **2u** (IC_{50} = *no effect* for both). No effect is defined as having IC_{50} greater than 100 μM (Fig. 3C).

As for the substituents at the phenyl ring, it was observed that shifting the chloro atom to the *meta* position generally resulted in mixed effects. Thus, comparing the two propyl derivatives **2k** and **2m**, the *meta* isomer (**2m**) showed equal activity, whereas the ethyl *meta* isomer **2f** was much more active than the *para* counterpart **2e** (Fig. 3C). Instead, the *ortho* chloro ethyl- and propyl- derivatives **2g** and **2l**, respectively, exhibited the same activity as the corresponding *meta* isomers **2f** and **2m**, respectively. A comparison of the inhibition activity of the *ortho* and *para* chloro isomers revealed that the *ortho* propyl **2l** was equally active as its *para* counterpart **2k**, while the *ortho* ethyl compound **2g** resulted in two times more activity than **2e**. Replacement of the chlorine in para position with fluoro and bromo atoms led to compounds showing different behavior, depending on the side chain. Thus, both ethyl-substituted fluoro and bromo compounds **2c** and **2d**, respectively, had a significant increase of inhibitory effect with respect to **2e**. In contrast, the propyl derivatives **2i** and **2j** showed similar activities with respect to their chloro counterpart **2k**. Finally, replacement of the chloro atom of **2e** with the amino substituent of **2h** led to an increase of activity (9.66 versus 5.91 μM) (Fig. 3C).

Altogether, the inhibition data described above indicates that the side chain is the portion that heavily affects the activity of compound **2** series, with C3 length having the highest activity. Longer or shorter side chains decreased the activity as well as the presence of cycloalkyl moieties. Polar portions attached to the side chains also led to a dramatic decrease in activity. Furthermore, the position of the chloro atom on the phenyl ring, as well as other halogens, did not cause substantial changes in the activity.

2.2.2. Effect on cellular activities – Uptake and nuclear transfer of EV cargoes

EVs, comprising exosomes and ectosomes, are nano-sized units involved in intercellular communication under both physiological and pathological conditions (see above) [34,35]. In cancer, the cellular transfer of EV cargoes, like oncoproteins and regulatory RNAs, alters the tumor microenvironment in ways that favor cancer growth and support neoangiogenesis [36–38], immunosuppression as well as cancer cell invasiveness and metastasis [39–41]. In such context, the VOR complex has been shown to play a central role in the nuclear transfer of cargo proteins transported by EVs based on a mechanism that relies on the translocation of $Rab7^+$ late endosomes containing endocytosed EVs into the NR, including deep nuclear membrane invaginations (NEIs) [18,19].

To visualize the impact of drugs on the endocytosis and nuclear transfer of cargo proteins carried by EVs, we exposed SW480 cells to fluorescently-tagged EVs produced by bioengineered SW620 cells expressing CD9-green fluorescent protein (GFP) [18]. We used the tetraspanin membrane protein CD9, as a marker of EVs. $CD9^+$ EVs played a positive (or negative) impact on malignancy depending on cancer type (reviewed in Ref. [42]). Thus, SW480 cells were first pre-treated for 10 min with 10 μM ICZ or a selected set of compounds (i.e. **1b**, **2a**, **2e**, **2j**, or **2s**) with high, medium or low/absent inhibition of the formation of VOR complex (see above). Afterward, $CD9\text{-}GFP^+$ EVs (1 x 10^9 particles per ml) were added to drug-treated cells and incubated for 5 h at 37 °C. The drugs were kept during this incubation. As solvent control, cells were treated with DMSO. Afterward, cells were washed, paraformaldehyde (PFA)-fixed, and then immunolabeled for Rab7 and SUN domain-containing protein 2 (SUN2) to highlight late endosomes and the inner nuclear membrane, respectively. Samples were analyzed by confocal laser-scanning microscopy (CLSM) through serial x-y optical sections (28–32 sections per cell) covering the entire cells of interest (see Supplementary Fig. S1). First, the impact of drugs on the subcellular localization of $Rab7^+$ late endosomes, with respect to their entry into NEIs, was assessed. We found that the transport of $Rab7^+$ late endosomes into $SUN2^+$ NEIs was significantly blocked in cells treated with ICZ, **2a**, and **2j**, but not in those incubated with **1b**, **2e** and **2s** (Fig. 4A, B). These data are consistent with their impact on VOR protein interactions, suggesting that later events are important for the former. Because late endosomes and NEIs provide a gateway for nuclear entry of EV cargo, co-localization of Rab7 and CD9-GFP was observed in the cytoplasmic compartment of cells treated with any drug, and in NEIs, at least for the control (DMSO) and inactive compounds (e.g., **2s**) that did not prevent translocation of late endosomes into NEIs (Fig. 4A). Consequently, the presence of CD9-GFP in the nucleoplasm was significantly reduced after the treatment with potent compounds (Fig. 4A, C). The causality effect is well illustrated with compound **2e** as its intermediate impact on ORP3-Rab7 interaction (IC_{50}: 10.55 μM) is reflected by its partial reduction of nuclear CD9-GFP (Fig. 4C). Finally, none of the chemical compounds interfered with EV endocytosis, as evidenced by the presence of CD9-GFP protein in the cytoplasmic compartment of all cells, just like the control (Fig. 4A, D). Therefore, these data demonstrate that certain drugs with a given formulation interfere with the nuclear transfer of EV cargoes (i.e. CD9-GFP), but not with the process of endocytosis, which is mirrored by their impact on the interaction of Rab7 with ORP3-VAP-A

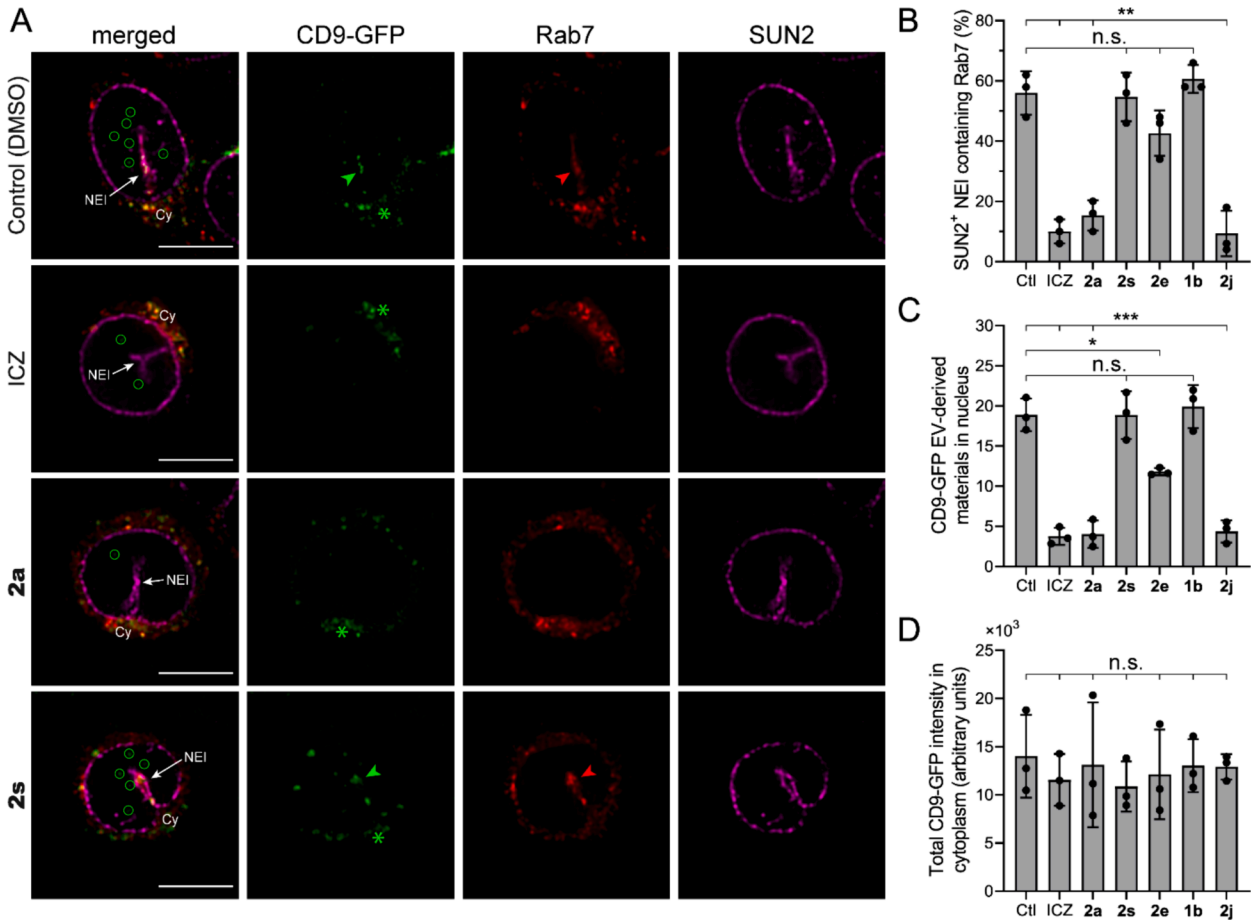

Fig. 4. ICZ and triazole derivative analogues inhibit the nuclear transport of EV-derived cargo. **A-D** SW480 cells were pretreated for 10 min with DMSO solvent alone (control, ctl) or with 10 μM ICZ, **2a**, **2s**, **2e**, **1b**, or **2j** prior to 5-hour incubation with CD9-GFP$^+$ EVs (1 x 10^9 particles/ml) in the absence (control) or presence of drugs. Cells were PFA-fixed and double immunolabeled for Rab7 and SUN2 prior to analysis by CLSM through serial x-y optical sections covering the entire cell of interest. A single section of interest from a representative cell is shown (A). In each cell, NEI is indicated by an arrow, while CD9-GFP and Rab7 signals within an NEI are indicated by green and red arrowheads, respectively. CD9-GFP signals in the cytoplasmic (Cy) and nucleoplasmic compartments are marked with green asterisks and circles, respectively. The presence of late endosomes in NEIs was quantified as the percentage of SUN2$^+$ NEIs containing Rab7 (B). The number of individual CD9-GFP spots in the nucleus (C) and the total CD9-GFP fluorescence intensity in the cytoplasm (D) were quantified. At least 50 NEIs (B) or 30 cells (C, D) were analyzed per independent experiment. Mean ± S.D. are shown and individual values for each experiment ($n = 3$) are shown. Note that endocytosis of CD9-GFP$^+$ EVs was not significantly affected by any drug (D). N.s, not significant. *, $p < 0.05$. **, $p < 0.01$. ***, $p < 0.001$. Scale bars, 10 μm. (For interpretation of the references to colour in this figure legend, the reader is referred to the web version of this article.)

complexes.

2.2.3. *Effect on cellular activities – Nuclear transfer of HIV-1 components and productive infection*

Considering the similarities between exosomal pathways and the retroviral cycle, as postulated by the Trojan exosome hypothesis [14–16,43,44], we investigate whether the new chemical compounds could also inhibit nuclear entry of virus components as those carried by HIV-1. Indeed, we have recently shown that both ICZ and compound **2a** can block the transport of endocytosed HIV-1 particles into NEIs, which then inhibits productive infection [17]. To evaluate the inhibitory effect of the new compounds on viral infection, we used a single replicating HIV-1 virus, pseudotyped with the vesicular stomatitis virus G (VSV-G) protein, and HeLa cells as host [17,45]. The HIV-1 clone comprises a frame-shift mutation in the *env* open reading frame, thus requiring co-expression with an envelope protein, in this case VSV-G, to generate infective virions (hereafter HIV-Gag-iGFP). The clone also carries GFP that is located between the matrix and capsid domains of the Gag protein and is therefore expressed only after productive infection. As recently reported [17], we induced the ectopic expression of Rab7-red fluorescent protein (RFP) in HeLa cells to monitor the endocytosis of viral particles. As proof-of-concept, we incubated Rab7-RFP$^+$ HeLa cells with compound **2a** (10 μM), or equivalent DMSO concentration as solvent control, for 30 min prior to 1-hour infection with HIV-Gag-iGFP. After methanol-fixation, infected cells were double immunolabeled for HIV-1 integrase (IN-2) and SUN2 and analyzed by CLSM. Under these conditions, IN-2 was found in part in Rab7-RFP$^+$ late endosomes distributed throughout the cytoplasmic compartment in both control and drug-treated cells (Fig. 5A, Pearson's R correlation coefficients: 0.81 ± 0.09 and 0.78 ± 0.10, respectively, $n = 10$). However, and consistent with our recent observation [17], Rab7-RFP$^+$ late endosomes containing IN-2 were absent from NEIs after drug treatment, indicating that compound **2a** inhibits nuclear entry of HIV-1 components, which is essential for productive infection.

Because HIV-1 entry into NEIs and interactions between VOR proteins are common cellular and molecular pathways leading to productive HIV-1 infection [17], we investigated the impact of compounds **1b**, **2e**, **2j**, **2p** or **2s** on productive infection. Again, ICZ and **2a** were used as positive controls and DMSO as a negative control. To this end, HeLa cells were incubated with different concentrations (2.5–10 μM) of drugs for 30 min before a 6-hour viral infection. The media were then replaced, and cells were further incubated for 24 h in the presence of the drugs. Afterward, flow cytometry was used to monitor the GFP expression, which requires nuclear import of HIV-1 and nuclear export of RNA

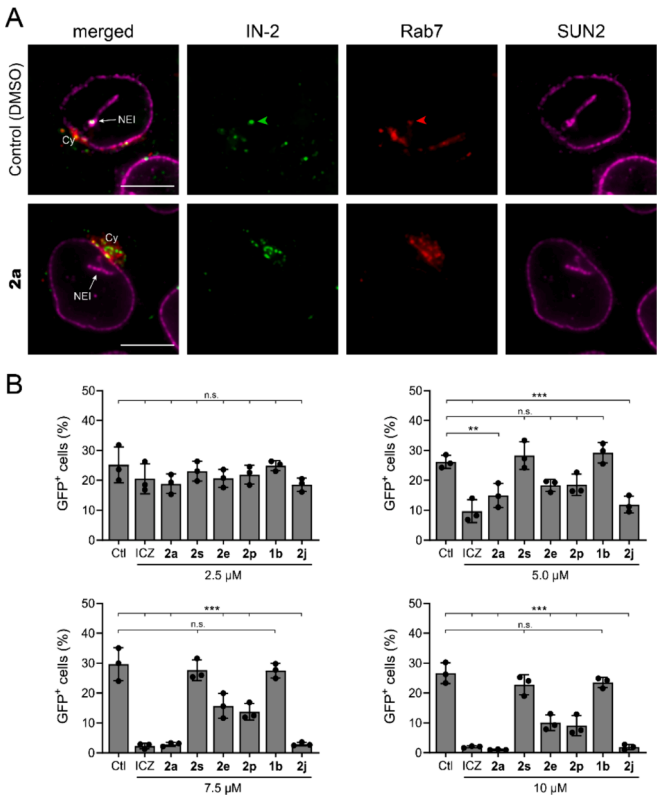

Fig. 5. Triazole analogues block productive HIV-1 infection. **A** HeLa cells expressing Rab7-RFP were pretreated with 10 μM of compound **2a** for 30 min before infection with HIV-Gag-iGFP pseudotyped with VSV-G for 1 h in the presence of drugs. DMSO was used as solvent control (Ctl). Cells were methanol-fixed and double immunolabeled for SUN2 and HIV-1 IN (IN-2) prior to analysis by CLSM through serial x-y optical sections covering the entire cell of interest. A single section of interest from a representative cell is shown. In each cell, NEI is indicated by an arrow, while IN-2 and Rab7-RFP (Rab7) signals within an NEI are indicated by green and red arrowheads, respectively. **B** HeLa cells were pretreated with various concentrations of ICZ or its analogues as indicated for 30 min prior to 6-hour infection. Afterward, they were incubated for 24 h in the presence of drugs. DMSO was used as solvent vehicle control. Cells were assessed by flow cytometry and the percentage of GFP^+ cells is presented. Means ± S.D. and individual values for each experiment ($n = 3$) are shown. Cy, cytoplasm. N.s., not significant. **, $p < 0.01$. ***, $p < 0.001$. Scale bars, 10 μm. (For interpretation of the references to colour in this figure legend, the reader is referred to the web version of this article.)

encoding Gag-iGFP. In line with data presented above, a progressive inhibition of productive infection was detected in cells treated with ICZ and analogues **2a**, and **2j**, with almost complete inhibition at 10 μM concentration (Fig. 5B). Likewise, **2e** and **2p** showed an intermediate inhibitory effect, while **1b** and **2s** showed no inhibition (Fig. 5B).

Altogether, data coming from endocytosis and nuclear transfer of cargo proteins studies in HIV-1-infected cells are in agreement with those obtained in SW480 cells after incubation with EVs, confirming the importance of side chain length for inhibitory activity. Compounds bearing a C3 alkyl chain (**2a, 2j**) showed results comparable to those obtained for ICZ, while compounds bearing *C*2 alkyl (**2e, 2p**), or cycloalkyl (**2s**) chains, or no chain (**1a**) revealed diminished activities or were completely inactive. In conclusion, these new compounds have the potential to block entry of HIV-1 viral components into the nucleus, thus hindering viral replication and subsequent productive infection.

2.2.4. Drug cytotoxicity

In view of the potential therapeutic use of some of the novel triazoles, we investigated their toxicity *in vitro* and *in vivo*. First, the impact of drugs on cell proliferation was evaluated using colorimetric assay (MTS reagent) using two distinct cell lines: cancer SW480 and normal fibroblast BJ cells. Sub-confluent cells were incubated for 48 h with different concentration (10–80 μM) of ICZ and triazole derivative analogues as indicated (Fig. 6). In comparison to control (DMSO), no significant effect was observed when 10 μM of drugs were applied and this for both cell lines (Fig. 6A). Only at higher concentrations (≥20 μM), a dose-dependent delay in cell growth was observed notably with fibroblast BJ cells (Fig. 6A). Second, the cytotoxic effect was evaluated in mice. A total of eight mice, two males and two females C57Bl/6 mice (four-months-old) were assigned to each control and treatment group. Mice were injected intraperitoneally daily with **2a** (200 mg/Kg) or an equivalent concentration of DMSO as solvent control for three weeks. We decided to use a dose of 200 mg/Kg corresponding to the highest dose of ICZ safely employed in mice [46]. Preliminary pharmacokinetics of **2a** in mice indicate that a concentration above 10 μM is achieved in mice for at least 8 h (A.l. et al., unpublished data). The body weight and hematological parameters of mice were than measured every week. No indication of drug-related cytotoxic effect on body mass was detected in our treatment group as we did not observe a significant change in both the control and treated group during the treatment period (Fig. 6B). Additionally, no clinical or biochemical abnormalities as well as no mortality was observed in either group (data not shown). Then, the hematological analysis was performed to assess the drug-induced myelosuppression effect of our treatment. To that end, we used a commercial BC-3600 Auto Hematology Analyzer [47]. Analysis of peripheral blood cell counts showed no significant changes in the level of red and white blood cells as well as platelets throughout the treatment course between the groups (Fig. 6C).

2.2.5. Molecular docking studies

To investigate the chemical interactions which underpin the data observed in the immunoisolation and immunoblotting of the three proteins of the VOR complex, docking simulations were performed on the homology model of the ORD of human ORP3 generated using the structure of ORP1 in complex with cholesterol [48], as described in the Experimental section. We applied the computational procedure based on the PLANTS docking software [49]. The obtained results confirm the interaction pattern already described for **1a** and **2a** and allow a better exploration of the role played by the specific substructures of these analogues [18]. As schematized above (Fig. 2), the structure of the simulated compounds can be subdivided into three regions: (1) the phenyl ring (red circle); (2) the triazole nucleus (green circle) and (3) the *N*-linked group (yellow circle).

In the simulated ligands, the phenyl ring assumes a common pose which is stabilized by a clear π-π interaction with Trp653 reinforced by a charge transfer interaction with Arg558 (Fig. 7). The halogen substituents can be involved in halogen bonds with Ser688 plus hydrophobic interactions with surrounding apolar side chains (e.g., Ile664 and Ile690). In agreement with biological data, docking results reveal that ortho, meta and para substitutions afford satisfactory and rather comparable results regardless of the added halogen atom. In all cases, the halogen atoms are involved in hydrophobic contacts without interfering with the key interactions stabilizing the complex and the corresponding computed complexes exhibit superimposable poses for the various halogenated compounds. For instance, the halogen atom in the ortho position of **2l** approaches Ile664 and Pro666 without hampering the contacts stabilized by the phenyl ring (Fig. 7A). Also, the *ortho*-chlorine atom can be also engaged in a halogen bond with Ser688. The additional interaction with Ser688 can also explain the increase of activity observed for the *meta* isomer **2f**. While considering the role played here by hydrophobic contacts, the interaction with Ser688 can also elucidate the good activity of the amino derivative **2h** compared to **2e**. Its putative complex can assume a slightly shifted pose by which the amino group can contact Ser688, while retaining the same pattern of key interactions described for the other derivatives (Fig. 7B).

In all modelled complexes (Fig. 7), the triazole ring, which is

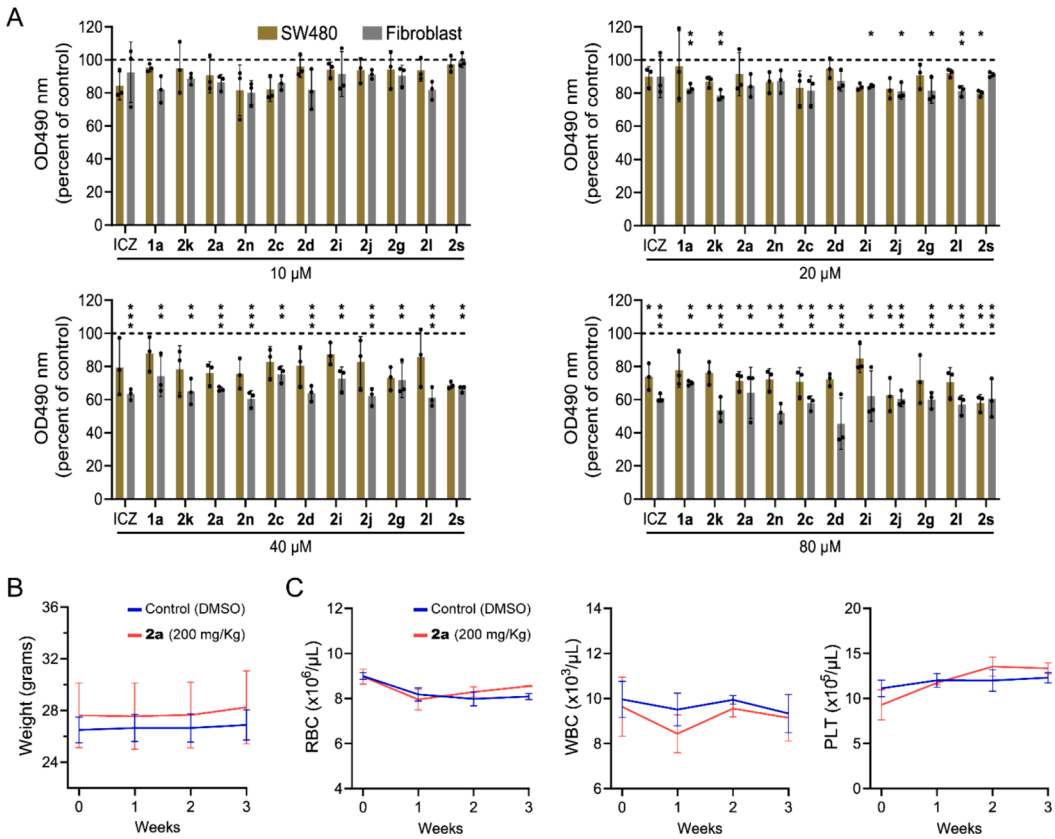

Fig. 6. Effects of ICZ and its smaller triazole derivative analogues on cell growth, mouse body weight and blood cell counts. **A** SW480 and fibroblast BJ cells were incubated with various concentrations of ICZ and drug analogues as indicated for 48 h. DMSO was used as solvent vehicle control. MTS tetrazolium compound was then added for 2 h to evaluate the amounts of viable cells. The absorbance value was measured at 490 nm. Data were normalized to the control (dashed line). Means ± S.D. are shown ($n = 3$). **B, C** No significant changes in body weight (B) of C57Bl/6 mice nor differences in peripheral blood cell counts (C) were observed after intraperitoneal (i.p.) injection of compound **2a** every 24 h for 3 weeks compared to DMSO control. RBC, red blood cells; WBC, white blood cells; PLT, platelets. *, $p < 0.05$. **, $p < 0.01$. ***, $p < 0.001$. (For interpretation of the references to colour in this figure legend, the reader is referred to the web version of this article.)

constantly included in all compounds, stabilizes a set of interactions in agreement with what was previously described [18]. In detail, this elicits H-bonds with Arg558 and Tyr593 as well as, to a minor extent, with Ser595, Ser596 and Ser688. The triazole ring also stabilizes π-π interactions with Tyr593 and Trp653 plus apolar contacts with surrounding alkyl side chains such as Leu559, Val651 and Pro666.

A greater structural variability is offered by the *N*-linked groups. Overall, docking results confirm the key role of this substituent which acts as a pivot to drive the ligand within the binding pocket and to assume the optimal arrangement. Thus, docking results emphasize that the derivatives devoid of this group show a wide variety of poses and are substantially unable to assume the optimal arrangement. For simplicity, the simulated ligands can be subdivided according to the polarity of this moiety. The first group comprises ligands bearing fully hydrophobic moieties, while the second group includes ligands with *N*-linked groups of different polarities.

Docking results evidence that the completely apolar *N*-linked groups are accommodated in the deepest region of the binding site where they can approach the above-cited hydrophobic residues (Leu559, Val651 and Pro666). Due to the limited size of this sub-pocket, one may understand why this group must be flexible and with a finely modulated steric hindrance. Thus, a propyl chain seems to have the optimal length and flexibility to be properly accommodated within this region, shorter and longer chains have a negative impact while ramified or cyclic groups are less tolerated. Docking results agree with these considerations since bulky *N*-linked moieties constrain the ligand to assume more external poses in which the triazole and phenyl rings lose most of their key contacts. Also, shorter alkyl chains are less effective in driving the ligand within the binding site and indeed the frequency and the ranking of the satisfactory poses decrease with the ethyl chain, almost disappearing with the methyl group.

Polar *N*-linked moieties have a generally negative impact and often induce a complete loss of inhibition activity. Nevertheless, some ligands show an intermediate activity that can be rationalized by docking simulations. In detail, terminal hydroxyl functions seem to be suitably tolerated and docking results reveal that these ligands can assume satisfactory poses in which the hydroxyl group stabilizes H-bonds with Ser595 and Ser596 as seen for **2q** (Fig. 7C). Among the ligands bearing a heterocycle in the *N*-linked moiety, only **2r** shows a modest inhibitory activity. The corresponding computed complex and highlights that **2r** assumes the expected pose and the protonated piperidine ring is engaged in an ion-pair with Glu562 (Fig. 7D). However, this relevant salt bridge does not exert the expected enhancing effect on the inhibition activity, and this can be explained by considering that Glu562 is engaged by a strong ion-pair with Lys685 with which the piperidine ring elicits a repulsive contact. Compounds with bulkier and more polar *N*-linked moieties are completely inactive reasonably as they are unable to counterbalance with extended apolar contacts the negative effect exerted by the polar functions as seen in the morpholine derivatives.

Taken together, biological data and computational results emphasize that the cavity which harbors the *N*-linked moiety has a clear preference for hydrophobic residues; it can tolerate polar groups which seem to be involved in specific interactions with surrounding polar residues, without marked effects on the observed activity. Docking results suggest that approaching the Glu562–Lys685 ion pair, which characterizes the deepest part of the binding pocket, has an overall negative role. More in

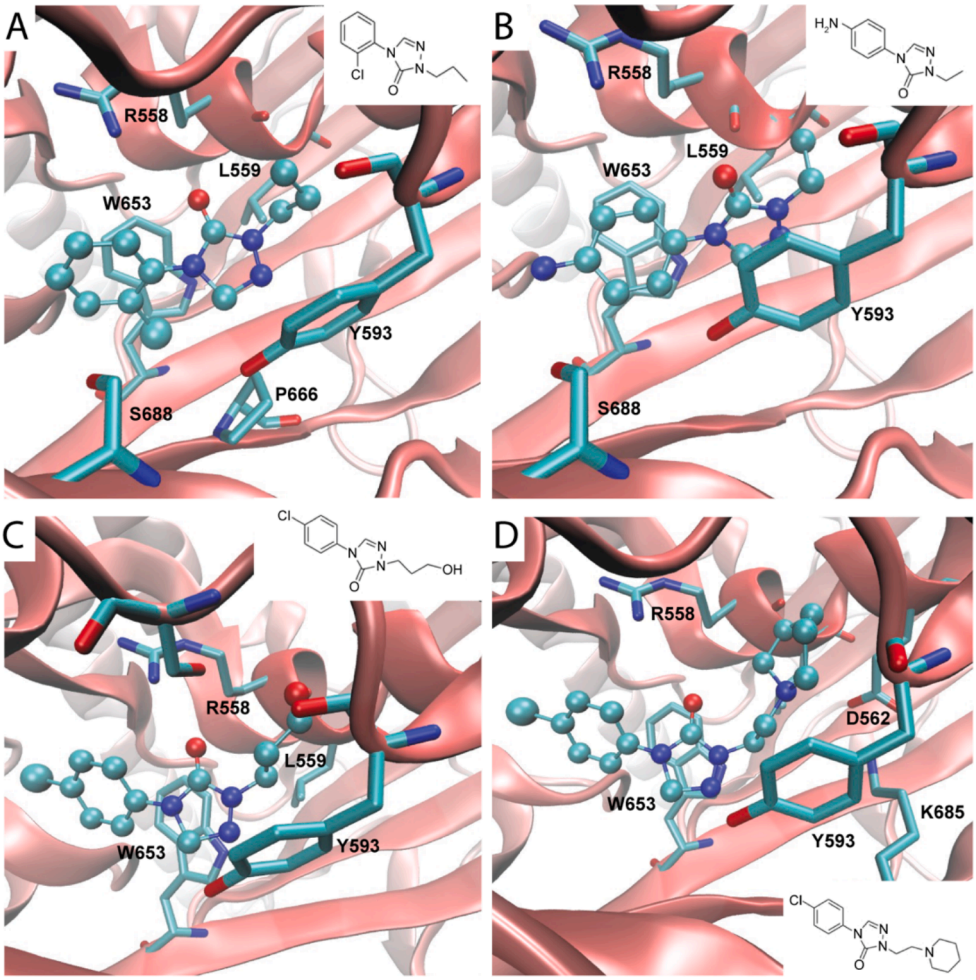

Fig. 7. Main interactions stabilizing the putative complexes of the ORP3 ORD with compounds **2l**, **2h**, **2q**, and **2r**. **A-D** These chemical analogue–ORP3 complexes were displayed to emphasize the beneficial role exerted by the *ortho*-chlorine atom (A, compound **2l**) and by the *para*-amino group (B, **2h**) as well as to rationalize the role played by a hydroxyl group on the *N*-linked substructure (C, **2q**) and by the ion-pair that the piperidine ring can elicit with Glu562 (D, **2r**). In the ribbon diagram of ORP3, the atoms were colored according to the CPK convention (nitrogen, blue; oxygen, red). Chemical analogues are presented using ball and stick model. (For interpretation of the references to colour in this figure legend, the reader is referred to the web version of this article.)

general, novel ligands could better investigate the possible roles of contacting Ser595, Ser596 and Ser688 since the available data evidence that stabilizing H-bonds can play beneficial roles (especially involving Ser688) provided that these additional interactions do not destabilize the key contacts involving the triazole nucleus. In particular, the rather similar activity of halogen and amino substitutions invites to better explore the chemical space of the phenyl moieties by adding diverse substituents which combine H-bonding capacity with a limited polarity.

It should be noted that the homology model used here including key residues involved in interactions with triazole derivative analogues is superposable with the AlphaFold predicted structure of human ORP3 ORD (Fig. 8A). It confirms the remarkable similarity between the two structures with a root-mean-square deviation of the backbone < 1 Å. The only variable part is the flexible lid modulating the site input (Fig. 8A). Computational results are generally in agreement with the experimental data and can be schematized (Fig. 8B). Along with the interactions stabilizing the phenyl ring and triazole nucleus and engaging an already reported triad of key residues (Arg558, Tyr593 and Trp653), docking results reveal that: (a) the optimal substituents for the phenyl ring are not too polar H-bonding group endowed with limited steric hindrance; (b) these substituents can be added in ortho, meta or para position with marginal differences; (c) the cavity, which harbors the *N*-linked moiety, has a clear preference for hydrophobic residues although it can tolerate polar groups that do not give rise to any beneficial effect on the activity

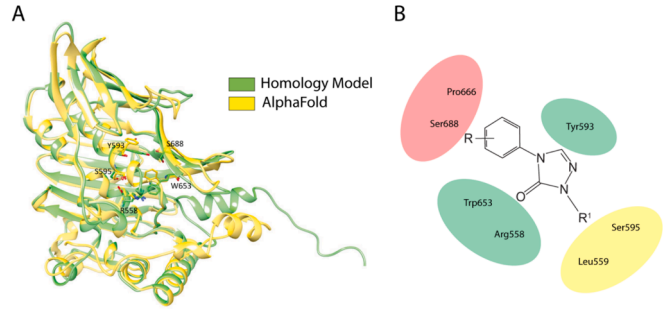

Fig. 8. Representation of key residues in ORP3 ORD involved in interactions with chemical drugs. **A** Comparison of the ORP3 ORD homology model (green) and that predicted by AlphaFold (yellow). The positions of residues involved in binding to inhibitors of the VOR complex are conserved. Only the flexible domain of the lid (i.e. the short *N*-terminal helix at the right part) covering the entrance to the hydrophobic pocket differs in the two models, as we have built our model on an open lid configuration (see Experimental Section). **B** 2D cartoon summarizing key ORP3 residues implicate in various interactions with inhibitors of the VOR complex. (For interpretation of the references to colour in this figure legend, the reader is referred to the web version of this article.)

in spite of the fact that they seem to be involved in specific interactions with surrounding polar residues.

All synthesized analogues including the larger ones (e.g., ICZ) are fitting within hydrophobic pocket of ORP3 ORD. Based on recent crystal structures of ORP3 ORD, questions were nonetheless raised for natural ligands such as cholesterol and 25-hc [50,51]. Although the total volume of the ORP3 ORD cavity is 2.6 times greater than that of the cholesterol, the shape of this pocket is not compatible with its tetracyclic rings. The latter contrast with experimental data showing that photo-analogues of cholesterol and 25-hc can bind to ORP3 [31]. Indeed, Suchanek and colleagues demonstrated that the full-length ORP3 bound to photo-analogues, but not the truncated protein carrying only the ORD [31], suggesting that the sterol-binding capacity of ORP3 might require the whole native protein, where the *N*-terminal part containing the PH domain and FFAT motif could influence the sterol-binding potential of ORP3, perhaps via their interactions with cellular components (e.g., endosomal membrane, VAP-A). These observations are in agreement with our previous data showing that 25-hc can suppress in a dose-dependent manner the negative action of ICZ or compound **2a** on VOR complex [18]. It remains to be determined whether post-translational modifications of ORP3 can alter (directly or indirectly) its conformation.

3. Conclusions

Compounds **2a-y**, having a triazolone structure, were efficiently synthesized by a two-step procedure in excellent overall yields (80–99 %). The synthesized compounds (except the intermediate **2y**) were evaluated as inhibitors of the Rab7 binding to ORP3–VAP-A complexes, and many of them showed, at a micromolar level, a remarkable ability to block the VOR complex formation and nuclear transport of EV and HIV-1 cargoes. An evaluation of the activity of the compound series **2** indicated that the side chain is the portion that plays a pivotal role in modulating the inhibitory effect of the triazolones. In fact, a C3 length is the most appropriate for good activity. On the other hand, a side chain one carbon longer (**2n**) reduces activity. The same applies to shorter, linear or methyl-branched side chains (**2e**, **2o**, **2b**). Cycloalkyl moieties (**2v**, **2w**, **2x**) and side chains bearing polar portions (**2p, 2q**) also dramatically decrease the inhibitory activity. The position of the chlorine group on the phenyl ring, as well as other halogens do not lead to substantial changes in the activity. At the biological level, the relationship between compound series 2-mediated inhibition of nuclear transfer of EV cargo or productive HIV-1 infection and translocation of their contents into the NR and VOR protein interactions suggest that inhibition of nuclear transport occurs at the level of the NR and involved Rab7-associated late endosomes, independently of the endocytosed particles (EVs or HIV-1).

Collectively, our investigation has refined the molecular determinants involved in the ORP3-drug binding site and provided a better understanding of the molecular and cellular mechanisms involved in the nuclear transfer of extracellular entities such as EV- and enveloped virus-cargoes. *In vivo* efficacy studies in cancer metastases, where the EVs can transform the physiological environment, and HIV-1 models are warranted.

4. Experimental section

4.1. Chemistry

All materials and solvents were purchased from commercial sources and used without further purification. All melting points were obtained on a Büchi-Tottoly capillary apparatus (Büchi, Cornaredo, Italy) and have not been corrected. IR spectra were determined in bromoform with a Shimadzu FT/IR 8400S spectrophotometer (Shimadzu Corporation, Milan, Italy). ^{1}H and ^{13}C spectra were measured at 200 and 50 MHz, respectively in DMSO-d_6 solution, using a Bruker Avance II series 200 MHz spectrometer (Bruker, Milan, Italy). Column chromatography was performed with Merck silica gel 230–400 mesh ASTM or with a Büchi Sepacor chromatography module (prepacked cartridge system). The HRMS of the final compounds acquired using a Thermo Q-Exactive system revealed a purity exceeding 95 %.

4.1.1. General synthesis of 1,2,4-triazol-3-ones 1 series

For the synthesis of 1,2,4-triazol-3-ones **1**, triethyl orthoformate (17.51 mmol, 2.9 ml), *p*-toluenesulfonic acid (1.5 mmol, 295 mg) and methyl carbazate (17.51 mmol, 1.6 g), were added to a solution of 4-chloroaniline (11.75 mmol, 1.5 g) in 100 ml methanol under nitrogen. The resulting reaction mixture was heated under reflux for 3 h. Once cooled at 20 °C a solution of sodium methoxide in methanol, prepared by addition of sodium (17.51 mmol, 403 mg) to methanol (30 ml), was added to the mixture that was heated under reflux for 2–24 h additional hours. The solvent was removed at reduced pressure and crushed ice was added to the reaction crude material. In case of compounds **1a**, **1c**, **1d**, **1f**, the resulting precipitate was filtered off and recrystallized from ethanol to afford the pure compounds. In case of compounds **1b** and **1e**, the reaction mixture was extracted in ethyl acetate (3x50 ml). The organic layers were dried over anhydrous Na_2SO_4, filtered and evaporated *in vacuo*. The resulting crude was purified by column chromatography to give the pure compounds.

4-(4-Chloro-phenyl)-2,4-dihydro-[1,2,4]*triazol-3-one* ***(1a)***. Conditions: 2 h at 50 °C, isolated by filtration and recrystallization in ethanol; white solid; yield: 99 %; Spectroscopic data were in accordance to those previously reported [18].

4-(2-Chloro-phenyl)-2,4-dihydro-[1,2,4]*triazol-3-one* ***(1b)***. Conditions: 24 h at reflux, isolated by extraction in ethyl acetate and purification by column chromatography using dichloromethane as eluent; white solid; yield: 85 %; mp: 200–201 °C; IR (cm^{-1}): 3325, 1698 (CO); ^{1}H NMR (200 MHz, DMSO-d_6) δ:, 7.49–7.52 (m, 1H), 7.52–7.53 (m, 1H), 7.56–7.57 (m, 1H), 8.11 (s, 1H), 11.95 (s, 1H, NH); ^{13}C NMR (50 MHz, DMSO-d_6) δ: 128.7 (d), 130.4 (d), 130.6 (d), 131.1 (s), 131.2 (d), 131.3 (s), 138.1 (d), 153.7 (s).

4-(4-Fluoro-phenyl)-2,4-dihydro-[1,2,4]*triazol-3-one* ***(1c)***. Conditions: 2 h at 50 °C, isolated by filtration and recrystallization in ethanol; white solid; yield: 99 %; mp: 239–240 °C (dec.); IR (cm^{-1}): 3305, 1702 (CO); ^{1}H NMR (200 MHz, DMSO-d_6) δ: 7.32–7.38 (m, 2H), 7.69–7.74 (m, 2H), 8.35 (s, 1H), 11.99 (s, 1H, NH); ^{13}C NMR (50 MHz, DMSO-d_6) δ: 116.5 (dx2, $J_{C3\text{-}F} = 22.9$ Hz), 124.42 (dx2, $J_{C2\text{-}F} = 8.6$ Hz), 130.9 (d $J_{C1\text{-}F} = 2.9$ Hz), 136.8 (d), 153.46 (s), 160.5 (d, $J_{C4\text{-}F} = 243.9$).

4-(4-Bromo-phenyl)-2,4-dihydro-[1,2,4]*triazol-3-one* ***(1d)***. Conditions: 2 h at 50 °C, isolated by filtration and recrystallization in ethanol; white solid; yield: 98 %; mp: 340–341 °C; IR (cm^{-1}): 3288, 1705 (CO); ^{1}H NMR (200 MHz, DMSO-d_6) δ: 7.55–7.59 (m, 2H), 7.76–7.80 (m, 2H), 8.12 (s, 1H), 10.64 (s, 1H, NH); ^{13}C NMR (50 MHz, DMSO-d_6) δ: 117.1 (s), 122.3 (dx2), 132.1 (dx2), 134.3 (d), 136.3 (s), 160.1 (s).

4-(4-Nitro-phenyl)-2,4-dihydro-[1,2,4]*triazol-3-one* ***(1e)***. Conditions: 4 h at 50 °C, isolated by extraction in ethyl acetate and purification by column chromatography using dichloromethane as eluent; white solid; yield: 98 %; mp: 242 °C; IR (cm^{-1}): 3095, 1705 (CO); ^{1}H NMR (200 MHz, DMSO-d_6) δ: 8.08 – 8.06 (m, 1H), 8.11 – 8.09 (m, 1H), 8.36 – 8.34 (m, 1H), 8.39 – 8.37 (m, 1H), 8.61 (s, 1H), 12.20 (s, 1H, NH); ^{13}C NMR (50 MHz, DMSO-d_6) δ: 121.3 (dx2), 125.4 (dx2), 136.0 (d), 140.1 (s), 145.4 (s), 153.0 (s).

4-(3-Chloro-phenyl)-2,4-dihydro-[1,2,4]*triazol-3-one* ***(1f)***. Conditions: 6 h at 50 °C, isolated by filtration and recrystallization in ethanol; white solid; yield: 89 %; mp: 220 °C; IR (cm^{-1}): 3327, 1639 (CO); ^{1}H NMR (200 MHz, DMSO-d_6) δ: 7.40 (dq, $J = 9.5$, 2.1, 1.0 Hz, 1H), 7.55 – 7.50 (m, 1H), 7.71 (dq, $J = 9.5$, 2.1, 1.0 Hz, 1H), 7.87 (t, $J = 2.0$ Hz, 1H), 8.45 (s, 1H), 12.06 (s, 1H); ^{13}C NMR (50 MHz, DMSO-d_6) δ: 120.0 (d), 121.3 (d), 127.0 (d), 131.4 (d), 134.0 (s), 135.9 (s), 136.4 (d), 153.2 (s).

4.1.2. General synthesis of compounds 2 series

To a solution of compounds **1** (4.1 mmol) in DMSO (10 ml), Na_2CO_3 (8.2 mmol, 869 mg), 18-crown-6 (4.1 mmol, 1.08 g) and the proper bromoalkane (5.33 mmol,) were added. In case of compound **2b**,

iodomethane was used as alkylating agent. The reaction mixture was heated at 60 °C for 3–6 h or alternatively under the refluxing temperature of the alkane for 6–24 h. Once cooled, distilled water was added and the mixture extracted with ethyl acetate (3 x 100 ml). The organic layers were dried over anhydrous Na_2SO_4, filtered and evaporated *in vacuo*. The crude material was purified by silica gel column chromatography using dichloromethane:ethyl acetate, 9:1 as eluent. In case of compounds **2a-d**, **2f-j**, **2l-o** and **2w-x**, after water addition, a precipitate was obtained. The subsequent filtration and recrystallization from ethanol allowed the isolation of the pure compounds.

4-(4-Chloro-phenyl)- 2-(1-methyl-propyl)-2,4-dihydro-[1,2,4]*triazol-3-one* ***(2a)***. Conditions: 3 h at 60 °C, isolated by filtration and recrystallization in ethanol; white solid; yield: 99 %; Spectroscopic data were in accordance to those previously reported by us [18]. HRMS: *m/z* [M + H]$^+$ calcd for $C_{12}H_{15}ClN_3O^+$ 252.08254 found, 252.08984.

4-(4-Chloro-phenyl)- 2-methyl-2,4-dihydro-[1,2,4]*triazol-3-one* ***(2b)***. Conditions: 3 h at 60 °C, isolated by filtration and recrystallization in ethanol; white solid; yield: 99 %; mp: 191–192 °C; IR (cm^{-1}): 1706 (CO); ^{1}H NMR (200 MHz, DMSO-d_6) δ: 3.39 (s, 3H, CH_3), 7.58 (d, J = 6.0 Hz, 2H), 7.75 (d, J = 6.0 Hz, 2H), 8.50 (s, 1H); ^{13}C NMR (50 MHz, DMSO-d_6) δ: 32.6 (q), 123.4 (d x 2), 129.8 (d x 2), 131.6 (s), 133.4 (s), 134.9 (d), 152.04 (s). HRMS: *m/z* [M + H]$^+$ calcd for $C_9H_9ClN_3O^+$ 210.03559; found, 210.04276.

4-(4-Bromo-phenyl)-2-ethyl-2,4-dihydro-[1,2,4]*triazol-3-one* ***(2c)***. Conditions: 3 h at 60 °C, isolated by filtration and recrystallization in ethanol; white solid; yield: 98 %; mp: 148–149 °C; IR (cm^{-1}): 1703 (CO); ^{1}H NMR (200 MHz, DMSO-d_6) δ: 1.25 (t, J = 7.2 Hz, 3H, CH_3), 3.77 (q, J = 7.2 Hz, 2H, CH_2), 7.67–7.74 (m, 4H), 8.50 (s, 1H); ^{13}C NMR (50 MHz, DMSO-d_6) δ: 14.1 (q), 30.1 (t), 119.9 (s), 123.7 (dx2), 132.7 (dx2), 133.9 (s), 134.9 (d), 151.0 (s). HRMS: *m/z* [M + H]$^+$ calcd for $C_{10}H_{11}BrN_3O^+$ 268.00072; found, 268.00801.

4-(4-Fluoro-phenyl)-2-ethyl-2,4-dihydro-[1,2,4]*triazol-3-one* ***(2d)***. Conditions: 3 h at 60 °C, isolated by filtration and recrystallization in ethanol; white solid; yield: 97 %; mp: 121–122 °C; IR (cm^{-1}): 1701 (CO); ^{1}H NMR (200 MHz, DMSO-d_6) δ: 1.26 (t, J = 7.2 Hz, 3H, CH_3), 3.77 (q, J = 7.2 Hz, 2H, CH_2), 7.34 –7.40 (m, 2H), 7.70 – 7.75(m, 2H), 8.44 (s, 1H); ^{13}C NMR (50 MHz, DMSO-d_6) δ: 14.2 (q), 30.2 (t), 116.6 (dx2, $J_{C3\text{-}F}$ = 22.9 Hz), 124.4 (dx2, $J_{C2\text{-}F}$ = 8.8 Hz), 130.9 (s), 135.3 (d), 151.3 (s), 159.4 (s), 161.0 (d, $J_{C4\text{-}F}$ = 244.1 Hz), 162.6 (s). HRMS: *m/z* [M + H]$^+$ calcd for $C_{10}H_{11}FN_3O^+$ 208.08079; found, 208.08795.

4-(4-Chloro-phenyl)-2-ethyl-2,4-dihydro-[1,2,4]*triazol-3-one* ***(2e)***. Conditions: 3 h at 60 °C, isolated by extraction in ethyl acetate and purification by gel column chromatography using dichloromethane: ethyl acetate, 9:1 as eluent; white solid; yield: 92 %; mp: 138–139 °C;IR (cm^{-1}): 1699 (CO); ^{1}H NMR (200 MHz, DMSO-d_6) δ: 1.26 (t, J = 7.2 Hz, 3H, CH_3), 3.75 (q, J = 7.2 Hz, 2H, CH_2), 7.59 (d, J = 8.7 Hz, 2H), 7.76 (d, J = 8.8 Hz, 2H), 8.49 (s, 1H); ^{13}C NMR (50 MHz, DMSO-d_6) δ: 14.1 (q), 40.2 (t), 123.4 (d x 2), 129.8 (d x 2), 131.7 (s), 133.8 (s), 135.0 (d), 151.5 (s). HRMS: *m/z* [M + H]$^+$ calcd for $C_{10}H_{11}ClN_3O^+$ 224.05124; found, 224.05855.

4-(3-Chloro-phenyl)-2-ethyl-2,4-dihydro-[1,2,4]*triazol-3-one* ***(2f)***. Conditions: 3 h at 60 °C, isolated by filtration and recrystallization in ethanol; yield: 88 %; mp: 78–79 °C; IR (cm^{-1}): 1702 (CO); ^{1}H NMR (200 MHz, DMSO-d_6) δ: 1.25 (t, J = 7.2 Hz, 3H, CH_3), 3.77 (q, J = 7.2 Hz, 2H, CH_2), 7.43 (ddd, J = 0.9, 2.1, 8.1 Hz, 1H), 7.53 (t, J = 8.1 Hz, 1H), 7.72 (ddd, J = 0.9, 2.1, 8.1 Hz, 1H), 7.87 (t, J = 2.0 Hz, 1H), 8.53 (s, 1H); ^{13}C NMR (50 MHz, DMSO-d_6) δ: 14.1 (q), 40.2 (t), 120.1 (d), 121.4 (d), 127.2 (d), 131.5 (d), 134.1 (s), 134.9 (d), 135.9 (s), 151.0 (s). HRMS: *m/z* [M + H]$^+$ calcd for $C_{10}H_{11}ClN_3O^+$ 224.05124; found, 0.224.05839.

4-(2-Chloro-phenyl)-2-ethyl-2,4-dihydro-[1,2,4]*triazol-3-one* ***(2 g)***. Conditions: 3 h at 60 °C, isolated by filtration and recrystallization in ethanol; yield: 86 %; mp: 85–86 °C; IR (cm^{-1}): 1708 (CO); ^{1}H NMR (200 MHz, DMSO-d_6) δ: 1.27 (t, J = 7.2 Hz, 3H, CH_3), 3.78 (q, J = 7.2 Hz, 2H, CH_2), 7.51–7.55 (m, 2H), 7.57–7.61 (m, 1H), 7.69–7.72 (m, 1H), 8.21 (s, 1H); ^{13}C NMR (50 MHz, DMSO-d_6) δ:14.2 (q), 30.1 (t), 128.8 (d), 130.4 (d), 130.7 (d), 131.2 (s), 131.2 (s), 131.4 (d), 136.6 (d), 151.6 (s). HRMS: *m/z* [M + H]$^+$ calcd for $C_{10}H_{10}ClN_3O^+$ 224.0540; found, 224.05859.

4-(4-Fluoro-phenyl)-2-propyl-2,4-dihydro-[1,2,4]*triazol-3-one* ***(2i)***. Conditions: 3 h at 60 °C, isolated by filtration and recrystallization in ethanol; white solid; yield: 99 %; mp: 107–108 °C; IR (cm^{-1}): 1703 (CO); ^{1}H NMR (200 MHz, DMSO-d_6) δ: 0.88 (t, J = 7.4 Hz, 3H, CH_3), 1.70 (q, J = 7.2, 2H, CH_2), 3.70 (t, J = 7.2 Hz, 2H, CH_2), 7.34–7.40 (m, 2H), 7.71–7.75 (m, 2H), 8.44 (s, 1H); ^{13}C NMR (50 MHz, DMSO-d_6) δ: 11.4 (q), 22.0 (t), 46.7 (t), 116.6 (d x 2, $J_{C3\text{-}F}$ = 23.0 Hz), 124.4 (d x 2, $J_{C2\text{-}F}$ = 8.6 Hz), 130.9 (d, $J_{C1\text{-}F}$ = 2.8 Hz), 135.3 (d), 151.7 (s), 161.0 (d, $J_{C4\text{-}F}$ = 244.1 Hz). HRMS: *m/z* [M + H]$^+$ calcd for $C_{11}H_{13}FN_3O^+$ 222.09644; found, 222.10359.

4-(4-Bromo-phenyl)-2-propyl-2,4-dihydro-[1,2,4]*triazol-3-one* ***(2j)***. Conditions: 3 h at 60 °C, isolated by filtration and recrystallization in ethanol; white solid; yield: 96 %; mp: 129–130 °C; IR (cm^{-1}): 1702 (CO); ^{1}H NMR (200 MHz, DMSO-d_6) δ: 0.88 (t, J = 7.4 Hz, 3H, CH_3), 1.66–1.73 (m, 2H, CH_2), 3.70 (t, J = 6.9 Hz, 2H, CH_2), 7.68–7.74 (m, 4H,) 8.50 (s, 1H); ^{13}C NMR (50 MHz, DMSO-d_6) δ: 11.4 (q), 21.9 (t), 46.7 (t), 119.9 (s), 123.7 (d x 2), 132.7 (d x 2), 133.9 (s), 134.9 (d), 151.4 (s). HRMS: *m/z* [M + H]$^+$ calcd for $C_{11}H_{13}BrN_3O^+$ 282.01637; found, 282.02329.

4-(4-Chloro-phenyl)-2-propyl-2,4-dihydro-[1,2,4]*triazol-3-one* ***(2k)***. Conditions: 6 h at 60 °C, isolated by extraction in ethyl acetate and purification by gel column chromatography using dichloromethane: ethyl acetate, 9:1 as eluent; white solid; yield: 98 %; mp: 135 °C; IR (cm^{-1}): 1702 (CO); ^{1}H NMR (200 MHz, DMSO-d_6) δ: 0.86 (td, J = 2.9, 7.4 Hz, 3H, CH_3), 1.64–1.71 (m, 2H, CH_2), 3.68 (t, J = 7.4 Hz, 2H, CH_2), 7.55–7.58 (m, 2H), 7.72–7.75 (m, 2H), 8.47 (s, 1H); ^{13}C NMR (50 MHz, DMSO-d_6) δ: 11.4 (q), 21.9 (t), 46.8 (t), 123.5 (d x 2), 129.8 (d x 2), 131.7 (s), 133.5 (s), 134.9 (d), 151.5 (s). HRMS: *m/z* [M + H]$^+$ calcd for $C_{11}H_{13}ClN_3O^+$ 238.06689; found, 238.07389.

4-(2-Chloro-phenyl)-2-propyl-2,4-dihydro-[1,2,4]*triazol-3-one* ***(2l)***. Conditions: 6 h at 60 °C, isolated by filtration and recrystallization in ethanol; yield: 83 %; mp: 77–78 °C; IR (cm^{-1}): 1705 (CO); ^{1}H NMR (200 MHz, DMSO-d_6) δ: 0.89 (t, J = 7.4 Hz, 3H, CH_3), 1.65–1.77 (m, 2H, CH_2), 3.70 (t, J = 6.8 Hz, 2H, CH_2), 7.49–7.61 (m, 3H), 7.69–7.72 (m, 1H), 8.21 (s, 1H); ^{13}C NMR (50 MHz, DMSO-d_6) δ: 11.3 (q), 22.1 (t), 46.8 (t), 128.8 (d), 130.4 (d), 130.7 (d), 131.3 (s), 131.3 (s), 131.4 (d), 136.6 (d), 152.0 (s). HRMS: *m/z* [M + H]$^+$ calcd for $C_{11}H_{13}ClN_3O^+$ 238.06689; found, 238.07412.

4-(3-Chloro-phenyl)-2-propyl-2,4-dihydro-[1,2,4]*triazol-3-one* ***(2 m)***. Conditions: 6 h at 60 °C, isolated by filtration and recrystallization in ethanol; yield: 90 %; mp: 155 °C; IR (cm^{-1}): 1698 (CO); ^{1}H NMR (200 MHz, DMSO-d_6) δ: 0.85–0.88 (m, 3H, CH_3), 1.66–1.73 (m, 2H, CH_2), 3.67–3.72 (m, 2H, CH_2), 7.44 (d, J = 8.0 Hz, 1H), 7.52–7.57 (m, 1H), 7.74 (d, J = 8.0 Hz, 1H), 7.89 (m, 1H), 8.56 (m, 1H); ^{13}C NMR (50 MHz, DMSO-d_6) δ: 11.4 (q), 21.9 (t), 46.8 (t), 120.0 (d), 121.3 (d), 127.2 (d), 131.5 (d), 131.1 (d), 134.8 (d), 135.9 (s), 151.4 (s). HRMS: *m/z* [M + H]$^+$ calcd for $C_{11}H_{13}ClN_3O^+$ 238.06689; found, 238.07402.

4-(4-Chloro-phenyl)-2-(1-methyl-butyl)-2,4-dihydro-[1,2,4]*triazol-3-one* ***(2n)***. Conditions: 6 h at 60 °C, isolated by filtration and recrystallization in ethanol; yield: 98 %; mp: 97–98 °C; IR (cm^{-1}): 1703 (CO); ^{1}H NMR (200 MHz, DMSO-d_6) δ: 0.86 (t, J = 7.4 Hz, 3H, CH_3), 1.16–1.23 (m, 2H, CH_2), 1.28 (d, J = 4.0 Hz, 3H, CH_3), 1.51–1.76 (m, 2H, CH_2), 4.17–4.29 (m, 1H), 7.56–7.61 (m, 3H), 7.75–7.81 (m, 2H), 8.50 (s, 1H); ^{13}C NMR (50 MHz, DMSO-d_6) δ: 14.0 (q), 19.3 (t), 20.0 q), 37.2 (t), 50.3 (d), 123.4 (d x 2). 129.7 (d x 2), 131.5 (s) 133.5 (s), 135.0 (d), 151.2 (s). HRMS: *m/z* [M + H]$^+$ calcd for $C_{13}H_{16}ClN_3O^+$ 265.09819; found, 265.01180.

4-(4-Chloro-phenyl)-2-isopropyl-2,4-dihydro-[1,2,4]*triazol-3-one* ***(2o)***. Conditions: 6 h at reflux, isolated by filtration and recrystallization in ethanol; yield: 99 %; mp: 115–116 °C (dec.); IR (cm^{-1}): 1709 (CO); ^{1}H NMR (200 MHz, DMSO-d_6) δ:1.31 (d, J = 4.0 Hz, 6H, 2xCH_3), 4.31–4.45 (m, 1H, CH), 7.58 (d, J = 8.9 Hz, 2H), 7.77 (d, J = 8.9 Hz, 2H), 8.50 (s, 1H); ^{13}C NMR (50 MHz, DMSO-d_6) δ: 0.6 (d), 21.4 (q), 46.7 (q), 123.4 (d x 2), 129.7 (d x 2), 129.8 (d), 131.6 (s), 133.5 (s), 150.7 (s). HRMS: *m/z*

[M + H]$^+$ calcd for $C_{11}H_{13}ClN_3O^+$ 238.06689; found, 238.07390.

4-(4-Chloro-phenyl)-2-hydroxyethyl-2,4-dihydro-[1,2,4]triazol-3-one ***(2p)***. Conditions: 24 h at reflux, isolated by extraction in ethyl acetate and purification by gel column chromatography using ethyl acetate, as eluent; yield: 87 %; mp: 114–115 °C; IR (cm^{-1}): 3450 (OH), 1701 (CO); ^{1}H NMR (200 MHz, DMSO-d_6) δ: 3.69–3.81 (m, 4H), 4.86 (d, J = 5.1 Hz, 1H), 7.62 (d, J = 8.5 Hz, 2H), 7.79 (d, J = 8.5 Hz, 2H), 8.53 (s, 1H); ^{13}C NMR (50 MHz, DMSO-d_6) δ: 48.0 (t), 58.8 (t), 123.4 (d x 2), 129.8 (d x 2), 130.0 (d), 131.6 (s), 133.6 (s), 152.0 (s). HRMS: m/z [M + H]$^+$ calcd for $C_{10}H_{11}ClN_3O_2^+$ 240.04615; found, 240.05343.

4-(4-Chloro-phenyl)-2-(3-hydroxy-propyl)-2,4-dihydro-[1,2,4]triazol-3-one ***(2q)***. Conditions: 3 h at 60 °C, isolated by extraction in ethyl acetate and purification by gel column chromatography using dichloromethane, as eluent; yield: 89 %; mp: 96–97 °C; IR (cm^{-1}): 3443 (OH), 1703 (CO); ^{1}H NMR (200 MHz, DMSO-d_6) δ: 1.79–1.88 (m, 2H), 3.43–3.49 (m, 2H), 3.80 (t, J = 7.1 Hz, 2H), 4.55 (t, J = 5.1 Hz, 1H), 7.59 (d, J = 8.7 Hz, 2H), 7.76 (d, J = 8.7 Hz, 2H), 8.50 (s, 1H). ^{13}C NMR (50 MHz, DMSO-d_6) δ: 31.9 (t), 42.6 (t), 58.4 (t), 123.4 (d x 2), 129.7 (d x 2), 129.8 (d), 131.6 (s), 133.5 (s), 151.4 (s). HRMS: m/z [M + H]$^+$ calcd for $C_{11}H_{13}ClN_3O_2^+$ 254.06180; found, 254.0688.

4-(4-Chloro-phenyl)-2-(2-piperidin-1-yl-ethyl)-2,4-dihydro-[1,2,4]triazol-3-one ***(2r)***. Conditions: 24 h at 90 °C, isolated by extraction in ethyl acetate and purification by gel column chromatography using ethyl acetate, as eluent; yield: 88 %; mp: 119–120 °C; IR (cm^{-1}): 1705 (CO); ^{1}H NMR (200 MHz, DMSO-d_6) δ: 135–1.44 (m, 6H), 2.36–2.37 (m, 4H), 2.57 (t, J = 6.7 Hz, 2H), 3.83 (t, J = 6.7 Hz, 2H), 7.59 (d, J = 8.8 Hz, 2H), 7.76 (d, J = 8.8 Hz, 2H), 8.50 (s, 1H); ^{13}C NMR (50 MHz, DMSO-d_6) δ: 24.4 (t), 26.0 (t x 2), 42.9 (t), 54.3 (t x 2), 56.8 (t), 128.3 (d x 2), 129.8 (d x 2), 130.0 (d), 131.6 (s), 133.5 (s), 151.6 (s). HRMS: m/z [M + H]$^+$ calcd for $C_{15}H_{20}ClN_4O^+$ 307.12474; found, 307.13138.

4-(4-Chloro-phenyl)-2-(3-piperidin-1-yl-propyl)-2,4-dihydro-[1,2,4]triazol-3-one ***(2s)***. Conditions: 24 h at 150 °C, isolated by extraction in ethyl acetate and purification by gel column chromatography using ethyl acetate, as eluent; yield: 90 %; mp: 116–117 °C; IR (cm^{-1}): 1701 (CO); ^{1}H NMR (200 MHz, DMSO-d_6) δ:1.34–1.48 (m, 6H), 1.80–1.87 (m, 2H), 2.30 (bs, 4H), 3.74–3.77 (t, J = 6.8 Hz, 4H), 7.59 (d, J = 8.7 Hz, 2H), 7.77 (d, J = 8.7 Hz, 2H), 8.49 (s, 1H); ^{13}C NMR (50 MHz, DMSO-d_6) δ: 24.5 (d), 25.8 (d), 25.9 (d), 43.8 (d x 2), 54.4 (d x 2), 56.1 (d), 123.3 (d x 2), 129.7 (d x 2), 129.8 (s), 131.6 (s), 133.5 (s), 151.4 (s). HRMS: m/z [M + H]$^+$ calcd for $C_{16}H_{22}ClN_4O^+$ 321.14039; found, 321.14709.

4-(4-Chloro-phenyl)-2-(2-morpholin-4-yl-ethyl)-2,4-dihydro-[1,2,4]triazol-3-one ***(2 t)***. Conditions: 24 h at 150 °C, isolated by extraction in ethyl acetate and purification by gel column chromatography using ethyl acetate, as eluent; yield: 94 %; mp: 129–130 °C; IR (cm^{-1}): 1702 (CO); ^{1}H NMR (200 MHz, DMSO-d_6) δ: 2.42 (bs, 4H), 2.62 (t, J = 6.5 Hz, 2H), 3.51–3.58 (m, 4H), 3.86 (t, J = 6.5 Hz; 2H), 7.59 (d, J = 8.6 Hz, 2H), 7.77 (d, J = 8.6 Hz, 2H), 8.51 (s, 1H); ^{13}C NMR (50 MHz, DMSO-d_6) δ: 42.4 (t), 53.5 (t x 2), 56.4 (t), 66.6 (t x 2), 123.4 (d x 2), 129.8 (d x 2), 129.8 (d), 131.7 (s), 133.5 (s), 151.6 (s). HRMS: m/z [M + H]$^+$ calcd for $C_{14}H_{18}ClN_4O_2^+$ 309.10400; found, 309.11063.

4-(4-Chloro-phenyl)-2-(3-morpholin-4-yl-propyl)-2,4-dihydro-[1,2,4]triazol-3-one ***(2u)***. Conditions: 2 h at 60 °C, isolated by extraction in ethyl acetate and purification by gel column chromatography using ethyl acetate, as eluent; yield: 93 %; mp: 101–102 °C; IR (cm^{-1}): 1707 (CO); ^{1}H NMR (200 MHz, DMSO-d_6) δ: 1.80–1.87 (m, 2H), 2.32–2.34 (m, 6H), 3.53–3.59 (m, 4H), 3.76–3.81 (m, 2H), 7.59 (dd, J = 2.3, 8.9 Hz, 2H), 7.77 (dd, J = 2.3, 8.9 Hz, 2H), 8.51 (s, 1H); ^{13}C NMR (50 MHz, DMSO-d_6) δ: 23.5 (t), 43.7 (t), 53.7 (t x 2), 55.9 (t), 66.7 (t x 2), 123.3 (dx2), 129.8 (dx2), 129.9 (d), 131.6 (s), 133.5 (s), 151.5 (s). HRMS: m/z [M + H]$^+$ calcd for $C_{15}H_{20}ClN_4O_2^+$ 323.11965; found, 323.12656.

4-(4-Chloro-phenyl)-2-cyclobutyl-2,4-dihydro-[1,2,4]triazol-3-one ***(2v)***. Conditions: overnight at 60 °C; yield: 97 %; white solid; mp: 125 °C; IR (cm^{-1}): 1703 (CO); ^{1}H NMR (200 MHz, DMSO-d_6) δ: 1.70–1.79 (m, 2H), 2.21–2.28 (m, 2H), 2.37–2.47 (m, 2H), 4.65–4.73 (m, 1H), 7.55–7.59 (m, 2H), 7.71–7.75 (m, 2H), 8.50 (s, 1H); ^{13}C NMR (50 MHz, DMSO-d_6) δ: 14.6 (t), 28.9 (t x 2), 48.7 (d), 123.7 (d x 2), 129.7 (d x 2), 131.7 (s), 133.4 (s), 135.2 (d), 150.6 (s). HRMS: m/z [M + H]$^+$ calcd for $C_{12}H_{13}ClN_3O^+$ 250.06689; found, 250.07418.

4-(4-Chloro-phenyl)-2-cyclopentyl-2,4-dihydro-[1,2,4]triazol-3-one ***(2w)***. Conditions: 24 h at 140 °C, isolated by filtration and recrystallization in ethanol; white solid; yield: 91 % mp: 142 °C; IR (cm^{-1}): 1704 (CO); ^{1}H NMR (200 MHz, DMSO-d_6) δ: 1.61 (bs, 2H), 1.79–1.91 (m, 4H), 1.94–1.99 (m, 2H), 4.51–4.60 (m, 1H), 7.58 (d, J = 8.8 Hz, 2H), 7.75 (d, J = 8.8 Hz, 2H), 8.48 (s, 1H); ^{13}C NMR (50 MHz, DMSO-d_6) δ: 24.5 (t x 2), 31.3 (t x 2), 55.5 (d), 123.5 (d x 2), 129.7 (d x 2), 131.6 (s), 133.5 (s), 134.8 (d), 150.9 (s). HRMS: m/z [M + H]$^+$ calcd for $C_{13}H_{15}ClN_3O^+$ 264.08254; found, 264.08975.

4-(4-Chloro-phenyl)-2-cyclohexyl-2,4-dihydro-[1,2,4]triazol-3-one ***(2x)***. Conditions: 3 h at 60 °C, isolated by filtration and recrystallization in ethanol; yield: 91 %; mp: 199–200 °C; IR (cm^{-1}): 1705 (CO); ^{1}H NMR (200 MHz, DMSO-d_6) δ: 1.19–1.44 (m, 4H), 1.64–1.83 (m, 6H), 3.98 (t, J = 3.7 Hz, 1H), 7.58 (d, J = 8.7 Hz, 2H), 7.76 (d, J = 8.7 Hz, 2H), 8.48 (s, 1H); ^{13}C NMR (50 MHz, DMSO-d_6) δ: 25.3 (t x 2), 31.5 (t x 2), 40.0 (t), 53.8 (d), 123.5 (d x 2), 129.7 (d x 2), 129.8 (d), 131.6 (s), 133.5(s), 150.7 (s). HRMS: m/z [M + H]$^+$ calcd for $C_{14}H_{16}ClN_3O^+$ 278.09819; found, 278.10406.

2-Ethyl-4-(4-nitro-phenyl)-2,4-dihydro-[1,2,4]triazol-3-one ***(2y)***. Conditions: 3 h at 60 °C, isolated by filtration and recrystallization in ethanol; white solid; yield: 98 %; mp: 222 °C; IR (cm^{-1}): 1706 (CO); ^{1}H NMR (200 MHz, DMSO-d_6) δ: 1.26 (t, J = 7.2 Hz, 3H, CH_3), 3.79 (q, J = 7.2 Hz, 2H, CH_2), 8.07–8.09 (m, 2H), 8.36–8.38 (m, 2H), 8.68 (s, 1H); ^{13}C NMR (50 MHz, DMSO-d_6) δ: 14.1 (q), 70.3 (t), 121.3 (d x 2), 125.5 (d x 2), 134.5 (d), 140.0 (s), 145.6 (s), 150.8 (s).

4.1.3. Synthesis of 4-(4-amino-phenyl)-2-ethyl-2,4-dihydro-[1,2,4]triazol-3-one 2 h

To a solution of compound **2y** (1.9 mmol, 0.5 g) in concentrated HCl (10 ml), tin chloride (11.4 mmol, 2.6 g) was added in portions. The reaction mixture was stirred at room temperature for 2 h. Then a solution of aqueous 30 % NaOH was added to the mixture up to pH 7. The formed precipitate was filtered off. Subsequent recrystallization in ethanol afforded the pure compound **2 h**. Yield: 90 %; mp: 108–109 °C; IR (cm^{-1}): 3446, 3361(NH_2), 1707 (CO); ^{1}H NMR (200 MHz, DMSO-d_6) δ: 1.23 (t, J = 7.2 Hz, 3H, CH_3), 3.70–3.77 (m, 2H, CH_2), 5.31 (s, 2H, NH_2), 6.61 (d, J = 8.7 Hz, 2H), 7.18 (d, J = 8.7 Hz, 2H), 8.18 (s, 1H); ^{13}C NMR (50 MHz, DMSO-d_6) δ: 14.3 (q), 40.1 (t), 114.1 (d x 2), 122.8 (s), 124.3 (d x 2), 124.4 (d), 148.7 (s), 151.7 (s). HRMS: m/z [M + H]$^+$ calcd for $C_{10}H_{13}N_4O^+$ 205.10111; found, 205.1080.

4.2. Molecular modeling

Molecular docking simulations were performed as previously described [18]. Briefly, the homology model of the ORD of human ORP3 (Uniprot entry: Q9H4L5, OSBL3_HUMAN) was generated using the structure of ORP1 in complex with cholesterol (PDB Id: 5ZM5) as the template [48], which also allowed to derive the pose of the drugs within the hydrophobic sterol-binding pocket. Docking simulations were then carried out by using docking software PLANTS [49] and focusing the search on an 8 Å radius sphere around the bound drugs. Although the resolved structure of the human ORP3 ORD was meanwhile reported [50,51], we still preferred to utilize here the homology model because its backbone is perfectly superimposable to that of the experimental structure apart from the flexible lid domain, which assumes a closed conformation in the resolved structure thus hampering the overall accessibility of its binding pocket. In contrast, the homology model was generated with the lid domain in its open conformation (in analogy to the ORP1 structure) and the resulting binding pocket is well suited to accommodate even large ligands such as chemical drug ICZ. Of note, the homology domain of ORP3 ORD is superposable with the AlphaFold predicted structure of human ORP3 (AlphaFold Protein Structure Database, see https://alphafold.ebi.ac.uk/entry/Q9H4L5) [52,53], where all key residues involved in the binding of VOR complex

inhibitors are conserved in position.

4.3. Biology

4.3.1. Cell culture

Human HeLa (ATCC® CCL-2™), fibroblast BJ (ATCC® CRL-2522™), SW480 (CCL-228™), and 293 T (CRL-3216™) cells were obtained from the American Type Culture Collection (ATCC). CD9-GFP$^+$ SW620 cells were generated from previous studies [54]. SW480 and CD9-GFP$^+$ SW620 cells were cultured in RPMI-1640 medium (catalog number (#) 10–041-CV, Corning), while HeLa, fibroblast BJ, and 293 T cells were kept in DMEM (#11995065, Thermo Fisher Scientific). All cell culture media were supplemented with 10 % fetal bovine serum (FBS, #26140079), 2 mM L-glutamine (#25030081), 100 U/mL penicillin and 100 μg/mL streptomycin (#15140122), all from Thermo Fisher Scientific. Cells were incubated at 37 °C in a 5 % CO_2 humidified incubator. Cells were regularly verified for absence of mycoplasma contamination by either their staining with 4′,6-diamidino-2-phenylindole (DAPI; #D9542, Sigma-Aldrich) and visualization under a fluorescent microscope or polymerase chain reaction using the MycoSEQ™ Mycoplasma Detection Kit (#4460626, Thermo Fisher Scientific), according to the manufacturer's protocol.

4.3.2. Plasmids

The HIV NL4-3 Gag-iGFP ΔEnv (#ARP-12455) plasmid was obtained from the NIH HIV Reagent Program. It carries the full-length HIV-1 clone with a frame shift mutation in the *env* open reading frame [55]. In the latter construct, GFP is introduced between the matrix (MA) and capsid (CA) domains of the Gag protein, as denoted by i (interdomain) in iGFP. The expression plasmid PSF-CMV-VSVG obtained from Sigma-Aldrich (#OGS592) was used for VSV-G-pseudotyping of HIV-1 particles.

4.3.3. Transfection

The transient co-transfections of 293 T cells (4×10^6) growing on 100-mm culture dishes were performed with HIV NL4-3 Gag-iGFP ΔEnv and PSF-CMV-VSVG plasmids using lipofectamine 3000 (#L3000008, Thermo Fisher Scientific) in a 1 part DNA: 2 parts lipid ratio. Cells were incubated for 24 h, medium replaced, then incubated further for 48 h at 37 °C under 5 % CO_2 prior to the collection of HIV-Gag-iGFP virus (see below).

4.3.4. Baculovirus-based expression

The baculovirus-based BacMam 2.0 CellLight® Late Endosomes-RFP (#C10589, Thermo Fisher Scientific) was used to induce the expression of Rab7-RFP in HeLa cells, which highlight late endosomes. Viral particles were added at a concentration of 30 per cell for 24 h, as recommended by the manufacturer. Afterward, Rab7-RFP$^+$ HeLa cells were infected with HIV-Gag-iGFP virus.

4.3.5. HIV-1 production and titration

Conditioned culture medium of 293 T cells was spun at 500 × *g* for 5 min at 4 °C to collect viral particles after transfection with viral plasmids as described above. The supernatant was then passed through sterile 0.45-μm filter and concentrated by centrifugation at 3,000 × *g* for 30 min at 4 °C using a Macrosep® Advance Centrifugal Device 100K (#89131–992, VWR International). The resulting viral supernatant was aliquoted and stored at − 80 °C. To determine the titer, HeLa cells seeded on 24-well plate were infected with various dilutions of HIV-Gag-iGFP, incubated for 48 h, and analyzed by flow cytometry (see below). Wells with less than 40 % fluorescent-positive cells were considered for calculations. Titer was measured as transduction units (TU)/ml = (number of infected cells × %GFP-positive cells) / volume of viral stock used in ml. The calculated titer was 2.6×10^5 TU/ml. We used a multiplicity of infection (MOI) of 2 throughout this study.

4.3.6. Isolation of CD9-GFP$^+$ EVs

CD9-GFP$^+$ SW620 cells (250,000 cells) were cultured in serum-free DMEM/F12 (#11330032, Thermo Fisher Scientific) supplemented with 2 % B-27 supplement (#17504044, Thermo Fisher Scientific) on 6-well plates pre-coated with 20 μg/ml poly(2-hydroxyethyl methacrylate) (#P3932, Sigma-Aldrich) to prevent their attachment. After 72 h, the cell medium was processed by differential centrifugation to enrich the EVs therein. Briefly, medium was centrifuged sequentially at 300 (5 min), 1,200 (20 min), and then 10,000 (30 min) × *g* at 4 °C, collecting the supernatant each step. To pellet the EVS, the resulting supernatant was centrifuged at 200,000 × *g* for 60 min at 4 °C. The pellet was then resuspended in 200 μl PBS. The size and concentrations of EVs were determined by nanoparticle tracking analysis using ZetaView (Particle Metrix GmbH) according to the manufacturer's protocol. For details about the characterization of CD9-GFP$^+$ EVs see Ref. [54].

4.3.7. Immunoisolation and immunoblotting

SW480 cells were incubated for 5 h with various concentrations (2.5, 5.0, 7.5, and 10 μM) of ICZ and drug derivatives at 37 °C. As a control, cells were incubated with DMSO alone. They were then solubilized in pre-chilled lysis buffer (0.5 % Triton X-100, 150 mM NaCl, 50 mM Tris-HCl, pH 8.0, supplemented with Set III protease inhibitor cocktail (#539134, Calbiochem)) on ice for 30 min, followed by centrifugation (12,000 × *g*) for 10 min at 4 °C. Immunoisolations were performed on detergent cell lysates using a mouse monoclonal Ab directed against human ORP3 (clone D-12, #sc-398326, Santa Cruz Biotechnology) followed by Protein G-conjugated magnetic beads according to the manufacturer's protocols (#130–071-101, Miltenyi Biotec). Samples were applied to μ Columns (#130–042-701, Miltenyi Biotec) for magnetic separation. Materials retained in columns were washed (4x) with 1 ml lysis buffer and rinsed once with 20 mM Tris-HCl pH 7.5. Pre-heated (95 °C) sodium dodecyl sulfate (SDS) buffer (1 % SDS, 50 mM DTT, 1 mM EDTA, 10 % glycerol, 0.005 % bromophenol blue, 50 mM Tris-HCl, pH 6.8) was applied to the column to elute the bound fractions. In other experiments, detergent lysates were first prepared from SW480 cells then treated with drugs for 30 min on ice prior to immunoisolation.

Protein samples (15–20 μg) were separated onto a 4–20 % Tris-glycine precast gel (#4561095, Bio-Rad) along with the Trident pre-stained protein molecular weight ladder (#GTX50875, GeneTex), and transferred to a nitrocellulose membrane (#88018, Thermo Fisher Scientific) overnight at 4 °C. Membranes were incubated in a blocking buffer (PBS containing 1 % bovine serum albumin (BSA; #97061–420, VWR International) for 60 min at room temperature (RT), and then probed with Abs against ORP3 (#A304-557A, Bethyl Laboratories), VAP-A (#A304-366A, Bethyl Laboratories), or Rab7 (#ab137029, Abcam) for 90 min at RT. After three washing steps of 10 min each with PBS containing 0.1 % Tween 20 (washing buffer; VWR International), the membranes were incubated with appropriate Alexa Fluor™ 488-coupled secondary Abs (#A11070, Thermo Fisher Scientific) diluted in blocking buffer for 30 min at RT. The membranes were rinsed three times with washing buffer, and the antigen-Ab complexes were visualized using the iBright FL1000 imaging system (Thermo Fisher Scientific).

4.3.8. Immunocytochemistry

SW480 cells grown on 35-mm poly-D-lysine-coated glass-bottom dishes (#P35GC-1.5–14-C, MatTek Corporation) were treated with 10 μM ICZ or various smaller triazole derivative analogues for 10 min, then CD9-GFP$^+$ EVs (1×10^9 particles/ml) derived from CD9-GFP$^+$ SW620 cells [54] were added and incubated further for 5 h. Cells were washed with PBS, fixed in 4 % PFA in PBS for 15 min, washed twice with PBS, permeabilized with 0.2 % Tween 20 in PBS for 15 min, and blocked with 1 % BSA for 1 h at RT. They were then labeled with primary Abs against SUN2 (clone A-10, #sc-515330, Santa Cruz Biotechnology) and Rab7 (clone EPR7589, #ab137029, Abcam) for 60 min at RT, washed twice with PBS, incubated with appropriate fluorescent secondary Abs (Alexa

Fluor™ 647-coupled anti-mouse or Alexa Fluor™ 555-coupled anti-rabbit Abs (#A-21237 or #A-21428, respectively, Thermo Fisher Scientific) for 30 min, and washed twice prior to observation. All Abs were diluted in permeabilization buffer containing 1 % BSA.

Alternatively, drug-treated Rab7-RFP$^+$ HeLa cells were infected with HIV-Gag-iGFP for 1 h prior to fixation in pre-chilled 100 % methanol at − 20 °C for 10 min. Permeabilization and Ab labeling were done similarly as above. For HIV-1 integrase (IN) staining, we used mouse monoclonal anti-HIV-1 IN Ab (clone IN-2, #sc-69721, Santa Cruz Biotechnology). Samples were imaged in PBS using the Nanoimager high-resolution microscope (ONI, Oxford, UK) with 100X oil-immersion objective. Images were acquired under the same microscope settings for subsequent quantification of fluorescence signal using Fiji software [56]. To determine the nuclear EV-derived fluorescent materials, regions of interest (ROIs) were plotted around the nucleus and an automatic threshold generated by Fiji was applied. Positive signals in 28–32 individual x-y optical sections (4-μm each step) were counted using the "analyze particle" function. To measure cytoplasmic signal of CD9-GFP$^+$ EVs, ROIs were drawn around the cytoplasm, excluding the nuclear compartment, and the "measure" function on Fiji was then applied to determine the fluorescent signal of all optical sections. The total cell fluorescence was calculated as: integrated density – (area × background mean fluorescence).

4.3.9. Flow cytometry

HeLa cells seeded on 24-well plates were treated with various concentrations (2.5–10 μM) of ICZ or its analogues for 30 min and then infected with HIV-Gag-iGFP for 6 h, medium replaced, and incubated further for 24 h in the presence of drugs as described [17]. DMSO alone was used as solvent vehicle control. Cells were detached using Trypsin/EDTA solution (#25–052-CI, Corning Inc.) for 3 min, blocked by the addition of cell medium (see above), centrifuged at 200 × *g* for 5 min, and resuspended in PBS. They were then immediately analyzed on the CytoFlex flow cytometer system (Beckman Coulter). Detector gain was kept constant for all experiments. DMSO-treated cells without viral infection were used to gate the negative cell population. At least 100,000 events were acquired, and data were analyzed using FlowJo software (version 10.7.2, BD Life Sciences).

4.3.10. Growth inhibition assay

SW480 and fibroblast BJ cells were seeded at a density of 4×10^3 cells on 96-well plates and incubated overnight to allow their adhesion. They were then treated with various concentrations (10–80 μM) of ICZ or its analogues for 48 h at 37 °C. DMSO was used as control. Afterward, CellTiter96 AQueous One Solution Cell Proliferation Assay (1:5 dilution; #G3580, Promega) was added for 2 h at 37 °C. The reagent utilizes the biochemical reaction of a tetrazolium compound [3-(4,5-dimethylthiazol-2-yl)-5-(3-carboxymethoxyphenyl)-2-(4-sulfophenyl)–2H-tetrazolium, MTS] to produce a colored, soluble formazan product that is proportional to the number of live cells. The absorbance value was measured at 490 nm using the Varioskan Flash plate reader (Thermo Fisher Scientific).

4.3.11. Animal studies

A total of eight (four males and four females) four-month-old C57Bl/6 mice (strain #000664, RRID:IMSR_JAX:000664, Jackson Laboratory) were used to study the effect of the synthetized compound on their weight and hematological parameters. Mice were injected intraperitoneally with 200 mg/Kg of compound **2a** or equivalent concentration of DMSO as solvent control every 24 h for three weeks. Mice weight was measured weekly, and blood samples (maximum of 100 μl) were collected by submandibular puncture and analyzed in triplicates using the BC-3600 Auto Hematology Analyzer (Mindray). Briefly, 20 μl of blood was diluted in 780 μl of diluent (M−30D, Mindray), fed to the machine, and analyzed in prediluted mode in triplicate. In all studies, mice were randomly assigned to each experimental group, keeping equal ratio of male to female sex, and monitored daily for signs of discomfort. Animals were euthanized at the end of study. The protocol was approved with number TUN-20–2 M by the Institutional Animal Care and Use Committee prior to the start of experiments.

4.3.12. Statistical analysis

All experiments were carried out at least in triplicate. The error bars in the graphical data represent the mean ± standard deviation (S.D.) as indicated in the figure legends. Statistical significance was determined using a two-tailed Student's *t*-test or one-way ANOVA with Dunnett's multiple comparisons test, and p values < 0.05 were considered significant. All graphs were created using GraphPad Prism 9 (version 9.3.1).

5. Sources of funding

Research reported in this publication was supported by the National Cancer Institute of the National Institute of Health under Award N. R15CA252990 (to A.l.). The content is solely the responsibility of the authors and does not necessarily represent the official views of the National Institute of Health. This work was also partially supported by the following grant: PRIN2017 Prot. No. 2017E84AA4 (to P.D.).

Declaration of competing interest

The authors declare the following financial interests/personal relationships which may be considered as potential competing interests: The United Kingdom patent application GB2598624A (applicants: M.F.S., G.R., P.D., G.C., A.L. and Technische Universität Dresden (TUD); inventors: M.F.S., G.R., P.D., G.C., D.C. and A.L.), European patent application EP3864409A1 (applicants: M.F.S., G.R., A.L. and TUD; inventors; M.F.S., G.R., D.C. and A.L.) and United States provisional patent number US20210353616A1 (applicants: M.F.S., G.R., A.L. and TUD; inventors: M.F.S., G.R., D.C. and A.L.) are pending. The authors declare no other competing interests.

Acknowledgements

The HIV-1 NL4-3 Gag-iGFP ΔEnv Non-Infectious Molecular Clone (ARP-12455) contributed by Dr. Benjamin Chen, was obtained through the NIH HIV Reagent Program, Division of AIDS, NIAID, NIH.

Appendix A. Supplementary data

Supplementary data to this article can be found online at https://doi.org/10.1016/j.bioorg.2024.107589.

References

[1] A. Bobrie, M. Colombo, S. Krumeich, G. Raposo, C. Théry, Diverse subpopulations of vesicles secreted by different intracellular mechanisms are present in exosome preparations obtained by differential ultracentrifugation, J. Extracell. Vesicles 1 (2012) 18397.
[2] M. Yáñez-Mó, et al., Biological properties of extracellular vesicles and their physiological functions, J. Extracell. Vesicles 4 (2015) 27066.
[3] Corbeil, D. & Lorico, A. Exosomes, microvesicles, and their friends in solid tumors, in *Exosomes: A Clinical Compendium*. (eds. L. Edelstein, J. Smythies, P. Quesenberry & D. Noble) 39-80 (Academic Press, 2020).
[4] J.A. Welsh, D.C. Goberdhan, L. O'Driscoll, E.I. Buzas, et al., MISEV2023: From basic to advanced approaches, J Extracell Vesicles 13 (2024) e12404.
[5] M. Sheta, E.A. Taha, Y. Lu, T. Eguchi, Extracellular Vesicles: New Classification and Tumor Immunosuppression, Biology (Basel) 12 (2023) 110.
[6] M. Tkach, C. Théry, Communication by Extracellular Vesicles: Where We Are and Where We Need to Go, Cell 164 (2016) 1226–1232.
[7] J. Meldolesi, Exosomes and Ectosomes in Intercellular Communication, Curr. Biol. 28 (2018) R435–R444.
[8] G.O. Arena, et al., Horizontal Transfer of Malignant Traits and the Involvement of Extracellular Vesicles in Metastasis, Cells 12 (2023) 1566.
[9] J. Ratajczak, M. Wysoczynski, F. Hayek, A. Janowska-Wieczorek, M.Z. Ratajczak, Membrane-derived microvesicles: important and underappreciated mediators of cell-to-cell communication, Leukemia 20 (2006) 1487–1495.

[10] H. Valadi, et al., Exosome-mediated transfer of mRNAs and microRNAs is a novel mechanism of genetic exchange between cells, Nat. Cell Biol. 9 (2007) 654–659.
[11] X. Wang, L. Tian, J. Lu, I.O. Ng, Exosomes and cancer - Diagnostic and prognostic biomarkers and therapeutic vehicle, Oncogenesis 11 (2022) 54.
[12] M. Vahabi, et al., Thinking small to win big? A critical review on the potential application of extracellular vesicles for biomarker discovery and new therapeutic approaches in pancreatic cancer, Semin. Cancer Biol. 97 (2023) 50–67.
[13] W.H. Chang, R.A. Cerione, M.A. Antonyak, Extracellular Vesicles and Their Roles in Cancer Progression, Methods Mol. Biol. 2174 (2021) 143–170.
[14] S.J. Gould, A.M. Booth, J.E. Hildreth, The Trojan exosome hypothesis, PNAS 100 (2003) 10592–10597.
[15] A. Pelchen-Matthews, G. Raposo, M. Marsh, Endosomes, exosomes and Trojan viruses, Trends Microbiol. 12 (2004) 310–316.
[16] R.A. Badierah, V.N. Uversky, E.M. Redwan, Dancing with Trojan horses: an interplay between the extracellular vesicles and viruses, J. Biomol. Struct. Dyn. 39 (2021) 3034–3060.
[17] M.F. Santos, et al., HIV-1-induced nuclear invaginations mediated by VAP-A, ORP3, and Rab7 complex explain infection of activated T cells, Nat. Commun. 14 (2023) 4588.
[18] M.F. Santos, et al., Itraconazole inhibits nuclear delivery of extracellular vesicle cargo by disrupting the entry of late endosomes into the nucleoplasmic reticulum, J Extracell Vesicles 10 (2021) e12132.
[19] M.F. Santos, et al., VAMP-associated protein-A and oxysterol-binding protein-related protein 3 promote the entry of late endosomes into the nucleoplasmic reticulum, J. Biol. Chem. 293 (2018) 13834–13848.
[20] G. Rappa, et al., Nuclear transport of cancer extracellular vesicle-derived biomaterials through nuclear envelope invagination-associated late endosomes, Oncotarget 8 (2017) 14443–14461.
[21] D. Corbeil, et al., Uptake and Fate of Extracellular Membrane Vesicles: Nucleoplasmic Reticulum-Associated Late Endosomes as a New Gate to Intercellular Communication, Cells 9 (2020) 1931.
[22] F. Nakatsu, A. Kawasaki, Functions of Oxysterol-Binding Proteins at Membrane Contact Sites and Their Control by Phosphoinositide Metabolism, Front. Cell Dev. Biol. 9 (2021) 664788.
[23] E.R. Eden, The formation and function of ER-endosome membrane contact sites, Biochim. Biophys. Acta 1861 (2016) 874–879.
[24] W.A. Prinz, A. Toulmay, T. Balla, The functional universe of membrane contact sites, Nat. Rev. Mol. Cell Biol. 21 (2020) 7–24.
[25] V.M. Olkkonen, OSBP-Related Protein Family in Lipid Transport Over Membrane Contact Sites, Lipid Insights 8 (2015) 1–9.
[26] S. Raychaudhuri, W.A. Prinz, The diverse functions of oxysterol-binding proteins, Annu. Rev. Cell Dev. Biol. 26 (2010) 157–177.
[27] M. Lehto, et al., Targeting of OSBP-related protein 3 (ORP3) to endoplasmic reticulum and plasma membrane is controlled by multiple determinants, Exp. Cell Res. 310 (2005) 445–462.
[28] M. Weber-Boyvat, et al., OSBP-related protein 3 (ORP3) coupling with VAMP-associated protein A regulates R-Ras activity, Exp. Cell Res. 331 (2015) 278–291.
[29] S.E. Murphy, T.P. Levine, VAP, a Versatile Access Point for the Endoplasmic Reticulum: Review and analysis of FFAT-like motifs in the VAPome, Biochim. Biophys. Acta 1861 (2016) 952–961.
[30] M. Johansson, M. Lehto, K. Tanhuanpaa, T.L. Cover, V.M. Olkkonen, The oxysterol-binding protein homologue ORP1L interacts with Rab7 and alters functional properties of late endocytic compartments, Mol. Biol. Cell 16 (2005) 5480–5492.
[31] M. Suchanek, et al., The mammalian oxysterol-binding protein-related proteins (ORPs) bind 25-hydroxycholesterol in an evolutionarily conserved pocket, Biochem. J 405 (2007) 473–480.
[32] R. Liu, et al., Itraconazole suppresses the growth of glioblastoma through induction of autophagy: involvement of abnormal cholesterol trafficking, Autophagy 10 (2014) 1241–1255.
[33] J. Xu, Y. Dang, Y.R. Ren, J.O. Liu, Cholesterol trafficking is required for mTOR activation in endothelial cells, PNAS 107 (2010) 4764–4769.
[34] G. Raposo, W. Stoorvogel, Extracellular vesicles: exosomes, microvesicles, and friends, J. Cell Biol. 200 (2013) 373–383.
[35] A. Zijlstra, D. Di Vizio, Size matters in nanoscale communication, Nat. Cell Biol. 20 (2018) 228–230.
[36] C. Grange, et al., Microvesicles released from human renal cancer stem cells stimulate angiogenesis and formation of lung premetastatic niche, Cancer Res. 71 (2011) 5346–5356.
[37] N. Kosaka, et al., Neutral sphingomyelinase 2 (nSMase2)-dependent exosomal transfer of angiogenic microRNAs regulate cancer cell metastasis, J. Biol. Chem. 288 (2013) 10849–10859.
[38] J. Skog, et al., Glioblastoma microvesicles transport RNA and proteins that promote tumour growth and provide diagnostic biomarkers, Nat. Cell Biol. 10 (2008) 1470–1476.
[39] D. Hoshino, et al., Exosome secretion is enhanced by invadopodia and drives invasive behavior, Cell Rep. 5 (2013) 1159–1168.
[40] O. Schillaci, et al., Exosomes from metastatic cancer cells transfer amoeboid phenotype to non-metastatic cells and increase endothelial permeability: their emerging role in tumor heterogeneity, Sci. Rep. 7 (2017) 4711.
[41] F. Yang, et al., Monoubiquitination of Cancer Stem Cell Marker CD133 at Lysine 848 Regulates Its Secretion and Promotes Cell Migration, Mol. Cell Biol. 38 (2018) e00024–e00028.
[42] A. Lorico, M. Lorico-Rappa, J. Karbanová, D. Corbeil, G. Pizzorno, CD9, a tetraspanin target for cancer therapy? Exp. Biol. Med. (Maywood) 9 (2021) 1121–1138.
[43] L. Krishnamoorthy, J.W. Bess Jr., A.B. Preston, K. Nagashima, L.K. Mahal, HIV-1 and microvesicles from T cells share a common glycome, arguing for a common origin, Nat. Chem. Biol. 5 (2009) 244–250.
[44] E. Nolte-'t Hoen, T. Cremer, R.C. Gallo, L.B. Margolis, Extracellular vesicles and viruses: Are they close relatives? PNAS 113 (2016) 9155–9161.
[45] C. Aiken, Pseudotyping human immunodeficiency virus type 1 (HIV-1) by the glycoprotein of vesicular stomatitis virus targets HIV-1 entry to an endocytic pathway and suppresses both the requirement for Nef and the sensitivity to cyclosporin A, J. Virol. 71 (1997) 5871–5877.
[46] J. Kim, et al., Itraconazole, a commonly used antifungal that inhibits Hedgehog pathway activity and cancer growth, Cancer Cell 17 (2010) 388–399.
[47] G. Shu, H. Lu, H. Du, J. Shi, G. Wu, Evaluation of Mindray BC-3600 hematology analyzer in a university hospital, Int. J. Lab. Hematol. 35 (2013) 61–69.
[48] J. Dong, et al., Allosteric enhancement of ORP1-mediated cholesterol transport by PI(4,5)P2/PI(3,4)P2, Nat. Commun. 10 (2019) 829.
[49] O. Korb, T. Stutzle, T.E. Exner, Empirical scoring functions for advanced protein-ligand docking with PLANTS, J. Chem. Inf. Model. 49 (2009) 84–96.
[50] X. Dong, Z. Wang, S. Ye, R. Zhang, The crystal structure of ORP3 reveals the conservative PI4P binding pattern, Biochem. Biophys. Res. Commun. 529 (2020) 1005–1010.
[51] J. Tong, L. Tan, Y.J. Im, Structure of human ORP3 ORD reveals conservation of a key function and ligand specificity in OSBP-related proteins, PLoS One 16 (2021) e0248781.
[52] M. Varadi, et al., AlphaFold Protein Structure Database: massively expanding the structural coverage of protein-sequence space with high-accuracy models, Nucleic Acids Res. 50 (2022) D439–D444.
[53] J. Jumper, et al., Highly accurate protein structure prediction with AlphaFold, Nature 596 (2021) 583–589.
[54] M.F. Santos, et al., Anti-Human CD9 Fab Fragment Antibody Blocks the Extracellular Vesicle-Mediated Increase in Malignancy of Colon Cancer Cells, Cells 11 (2022) 2474.
[55] W. Hübner, et al., Sequence of human immunodeficiency virus type 1 (HIV-1) Gag localization and oligomerization monitored with live confocal imaging of a replication-competent, fluorescently tagged HIV-1, J. Virol. 81 (2007) 12596–12607.
[56] J. Schindelin, et al., Fiji: an open-source platform for biological-image analysis, Nat. Methods 9 (2012) 676–682.